LIMNOLOGY and OCEANOGRAPHY

ASLO

Limnol. Oceanogr. 9999, 2024, 1–13

doi: 10.1002/lno.12537

Internal wave resonance, surges, and strong nonlinear damping differentiated in two elongated lakes with the aid of an original Green's function

James P. Long [1], **John D. Halfman** [2*], **Nathan Hawley** [3]

[1]Finger Lakes Institute, Hobart and William Smith Colleges, Geneva, New York, USA
[2]Department of Geoscience and Environmental Studies Program, Hobart and William Smith Colleges, Geneva, New York, USA
[3]Great Lakes Environmental Research Laboratory, Ann Arbor, Michigan, USA

Abstract

While the analogy between the wind-pumped internal seiche in a lake and the driven damped-harmonic oscillator is recognized, use of a damped-oscillator model to understand internal-wave behavior is seldom attempted due to the irregular waveforms arising from variable winds, and to the presence of nonlinear waves like surges. Using a new variable-frequency Green's function derived for a damped oscillator within the context of the two-layer model of a stratified basin, we examine internal wave behaviors in Seneca and Owasco Lakes, two elongated lakes in New York state with very different lengths and depths. Our approach reproduces the measured undulations of the lowest horizonal-mode internal-seiche with surprising fidelity. It also yields the seiche's seasonal variation of frequency, primarily due to changes in the stratification intensity and thermocline depth. Notably, our model also estimates the seiche amplitude decay-time, a key quantity difficult to obtain for a constantly agitated seiche. The decay time matches the computed surge-formation time, which limits seiche lifetimes to as little as one seiche period. Surges also strongly affect the undulating internal-wave waveforms in a manner consistent with tank experiments. Finally, we find that the internal seiche in Owasco Lake exhibits a uniquely well-defined resonance with the diel wind pattern, and, for Seneca Lake, that surges propagate bidirectionally, augmenting an oft-cited report of surges traveling only in one direction.

The internal seiche in a stratified lake often degenerates into nonlinear internal waves (NLIWs) such as surges and bores propagating along the thermocline (Mortimer 1974; Boegman 2010; Maderich et al. 2012). Under such conditions, predictions of the undulations in the thermocline induced by variable winds generally use numerical codes, though important insights are available from analytical analysis and tank experiments. It has long been recognized that the internal-seiche standing-wave is analogous to a damped oscillator (Mortimer 1974; Fricker 2000), but with few exceptions (Imam et al. 2013*a*,*b*) the model has not been explicitly applied to field data. Here, we test the ability of a simple damped-harmonic oscillator model to describe the lowest horizontal-mode of the internal seiche (the H1 mode) using temperature observations from two elongated lakes that also simultaneously exhibit NLIWs. We treat the H1 mode as a damped oscillator within the context of the "two-layer model," that is, a rectangular basin discontinuously separated at the thermocline into an epilimnion floating atop a denser hypolimnion.

We first present the differential equation for a damped oscillator that represents the thermocline displacement over time, which we solve by convolving the measured wind stress with a new Green's function derived specifically to include the seasonally varying natural frequency $f_1(t)$. (A full table of symbols is provided in Supporting Information Tables S1 and S2.) The Green's function also includes a damping coefficient γ—the inverse of the amplitude $1/e$ damping time—which is not commonly extractable for constantly agitated internal waves. With $f_1(t)$ and γ employed as adjustable parameters, the model is successfully fitted to thermocline undulations inferred from temperature–depth profiles measured over the stratified season in Owasco and Seneca Lakes (2 of the 11 Finger

*Correspondence: halfman@hws.edu

Additional Supporting Information may be found in the online version of this article.

Author Contribution Statement: J.P.L. wrote the manuscript, and J.D.H. and N.H. provided field data and edited the manuscript.

Lakes in central New York) whose significantly different lengths and depths lead to distinctive behaviors with respect to nonlinear surges and wind-wave resonance. Both lakes are narrow enough to be relatively free from Coriolis effects (Gelda et al. 2015), making them suitable candidates for analysis within the two-layer picture of a narrow basin while also providing an opportunity to field-verify laboratory experiments.

Methods

Study sites

Seneca and Owasco Lakes (Fig. 1) occupy deep, glacially excavated, N-S trending basins about 37 km apart in central New York state, USA. Owasco Lake is ~ 17.9 km long, with a mean width of 1.5 km (maximum 2.1 km) and mean depth of 29.3 m (maximum 54 m). Seneca Lake is much larger, ~ 56 km long with a mean width of 3.1 km (maximum 5.2 km) and mean depth of 88.6 m (maximum 188 m) (Birge and Juday 1914). Owasco Lake is dimictic. Seneca Lake is typically warm monomictic.

Water column temperatures were measured at three sites in Seneca Lake (Fig. 1a; Table 1). The Finger Lakes Institute buoy (Fig. 1a, "FLI buoy"), a model YSI/Xylem 6952 with an EXO2 sonde, was deployed in 60 m of water near the northern end of the lake. It recorded temperature (accuracy 0.01°C) at ~ 1.5-m intervals (accuracy 0.04 m) as the sonde descended to 55 m every 12-h, a time resolution just sufficient to characterize the internal seiche. The data (FLI 2021*a*) were calibrated annually using weekly, in situ, SeaBird SBE25 profiles of temperature and depth (accurate to 0.002°C and 0.04 m) collected at four nearby sites in the northern end of the lake. The buoy also collected 5-min mean wind speed and direction data at half hour intervals with a RM Young (05106) anemometer 3.1 m above the lake surface (FLI 2021*a*). Data were also obtained from a platform deployed by the US Geological Survey (USGS Seneca 2021) to the north of the FLI Buoy, which measured temperatures every 15 min using a combination of Onset Pendant thermistors (0.5°C accuracy), and YSI EXO1 and EXO2 sondes at 1-m intervals down to 30 m (accurate to 0.01°C and 0.04 m).

The southernmost station on Seneca Lake was a thermistor string moored in the deepest basin of the lake that measured temperatures throughout the year (Fig. 1a, "National Oceanic and Atmospheric Administration's Great Lakes Environmental Research Laboratory [GLERL] mooring"). The portion of the string employed here was instrumented with a combination of Seabird SB39 and Onset HOBO U20, U22, and Tidbit sensors. The SB39 and Onset U20 sensors also measured water depth. Temperature accuracy ranged from 0.2°C to 0.4°C, and depth sensors were accurate to 0.1 m. The sensors were deployed at 2.5-m intervals from 5 to 20 m, 5-m intervals from 25 to 60 m, 10-m intervals from 70 to 120 m, and larger

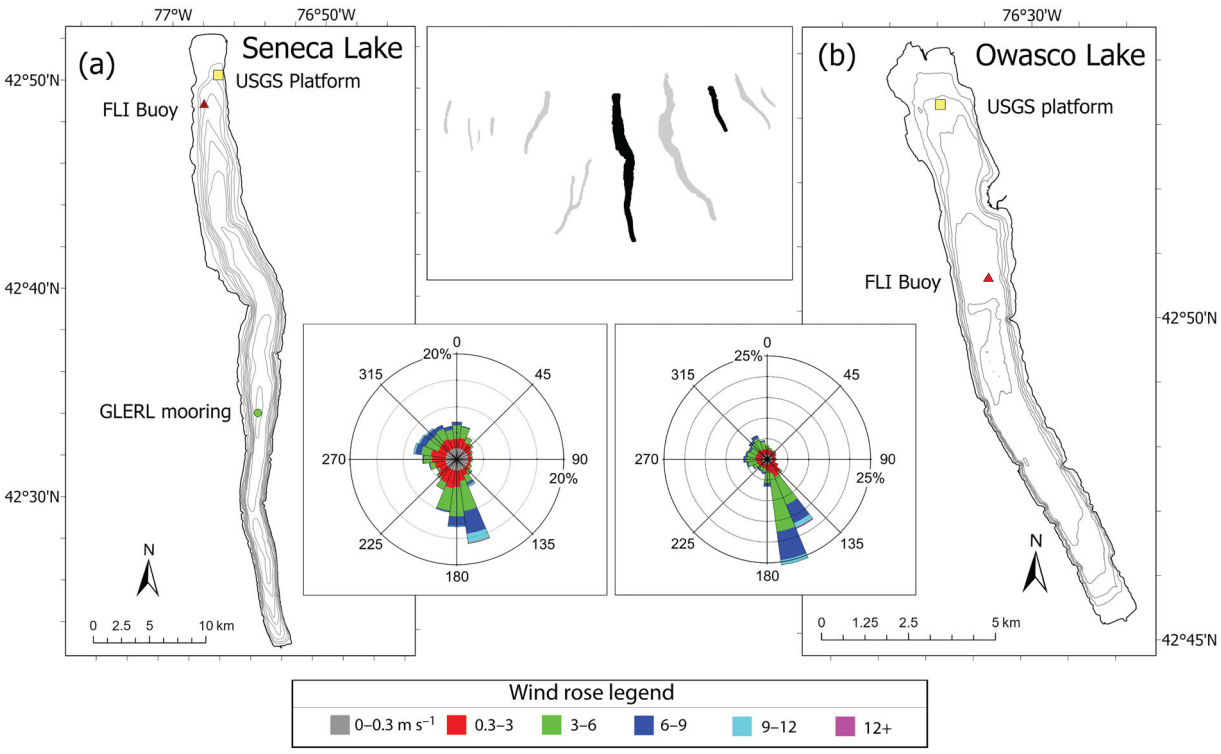

Fig. 1. Bathymetric maps for (**a**) Seneca Lake (20-m contours) and (**b**) Owasco Lake (10-m contours), with field stations marked. Note different length scales. Insets: site map of the Finger Lakes with the two studied lakes called out in black, and the wind rose for each lake over the stratified season, 2019 for Seneca Lake, and 2020 for Owasco.

Table 1. Station information and fitting conditions.

Lake	Station	Latitude	Longitude	Depth at station (m)	Deployed	Retrieved	Depth range measured (m)	Interval fitted
Seneca	FLI	42.8192°	−76.9436°	60	28 Apr 2019	19 Oct 2019	1–50	18 May 2019
								05 Oct 2019
Seneca	USGS	42.0849°	−76.7828°	30	15 May 2019	20 Oct 2019	1–26	15 May 2019
								11 Oct 2019
Seneca	GLERL	42.5542°	−76.9494°	178	12 Aug 2018	22 Aug 2019	2.5–50	31 May 2019
					22 Aug 2019	08 Dec 2019		15 Oct 2019
Owasco	FLI	42.8392°	−76.5142°	50	22 May 2020	24 Oct 2020	n/a	n/a
Owasco	USGS	42.8875°	−76.5317°	26	9 Jun 2020	22 Oct 2020	1–26	9 Jun 2020
								9 Oct 2020

intervals down to the lake floor at ∼ 178 m. Each August the sensors were retrieved and new ones deployed. In 2019, temperatures were measured every hour until August 22, and every 15 min thereafter. Sway in the moored cable episodically influenced the thermistor depths, but was accounted for with the pressure-to-depth transducers. This deployment was a collaboration between FLI and the GLERL.

Temperature-depth records for Owasco Lake (Fig. 1b, "USGS platform"; Table 1) were obtained from data measured at a USGS platform (USGS Owasco 2021). The platform was deployed in 26 m of water, and measured temperatures using Onset Pendant thermistors and YSI's EXO1 and EXO2 sondes every 15 min at 1-m intervals down to the lake floor. As at Seneca Lake, half hour wind speed and direction data were obtained from an RM Young (05106) anemometer mounted 3.1 m above the lake surface on an FLI buoy, a YSI/Xylem model 6951, deployed south of the USGS platform in 50 m of water (FLI 2021*b*).

Data processing

Table 1 gives the temporal and spatial ranges of the data used. All raw temperature-depth profiles were linearly interpolated to a spacing of 0.2 m. For depths between the surface and the uppermost sensor (Table 1), the temperature was assumed to be that of the uppermost sensor. Missing values in the time series were approximated by linear interpolation for a uniform spacing equal to the nominal sampling-time intervals for each station: 30 min for the wind measurements recorded by the FLI buoys, and for the recorded temperature profiles: 15 min for the USGS platforms, 12 h for FLI buoy, and 1 h for the GLERL moored cable.

We characterize internal waves at a given field station through the undulating displacement $\delta h(t)$ of the thermocline from its quasi-static depth, defined through three time-series in the relation $h(t) = h_{1qs}(t) + \delta h(t)$. Here $h(t)$ is the instantaneous depth of the thermocline at a site at time t, and $h_{1qs}(t)$ is the seasonally varying quasi-static depth of the thermocline. At each station, we determine the instantaneous thermocline depth $h(t)$ from the measured time-series $T(z, t)$ of a temperature profile (Supporting Information, Data Processing; Fig. S1); the results for $h(t)$ appear in Supporting Information Fig. S2. Our intention is to fit the damped-oscillator model to the first of the horizontal V1H*n* internal-seiche modes (Münnich et al. 1992), hereafter the H1 mode (we neglect vertical modes). However, the thermocline undulations $\delta h(t)$ contain contributions from higher H*n*-modes, as well as NLIWs that exhibit a broad frequency spectrum (Horn et al. 1986; Lemmin 1987; Boegman et al. 2005; Boegman and Ivey 2012). Therefore, in order to restrict the fitting mainly to the H1 mode, we filtered $h(t)$ through a low-pass filter with a frequency cutoff set to 1.5 times the highest expected H1 seiche frequency (Boegman et al. 2005). The filtered result, $h_{LP}(t)$, is the time series fitted with the damped-oscillator model. Because filtering leaves the slowly varying $h_{1qs}(t)$ intact, $h_{LP}(t) = h_{1qs}(t) + \delta h_{LP}(t)$, where $\delta h_{LP}(t)$ approximates the H1 undulations. As explained later, $\delta h_{LP}(t)$ also includes a contribution from surges recurring at the H1 frequency. The quasi-static $h_{1qs}(t)$ is returned automatically during fitting (Supporting Information Fig. S2).

Theory: The damped-oscillator/two-layer model

We assume that the amplitude of each internal-seiche horizontal mode behaves as a mechanical damped-oscillator driven by a force related to the surficial wind-stress. Specifically, we identify the displacement from equilibrium $\zeta_n(t)$ of the n^{th} damped oscillator with the contribution of the Hn^{th} mode to the vertical displacement of the thermocline from its quasi-static position at the endwall of the basin. The differential equation for the oscillator can be derived under reasonable approximations (Supporting Information, Equation of Motion) from a hydrostatic treatment by Heaps and Ramsbottom (1966) of the coupled surface- and internal-seiches within the two-layer model of a rectangular basin disturbed by a spatially uniform wind:

$$\ddot{\zeta}_n(t) + 2\gamma\dot{\zeta}_n(t) + \omega_n^2(t)\zeta_n(t) = \frac{4h_2}{\rho_2 LH}\rho_a C_D(t-t_0)U_{10}^2(t-t_0)\cos(\theta+\varphi) \quad (1)$$

The left-hand side of Eq. 1 is the differential equation for a damped oscillator (Thornton and Marion 2008), and the

right-hand side derives from the wind forcing. Here, single- and double-dots represent the first- and second-time derivatives, respectively; γ is a damping coefficient, assumed to be the same for each mode (Heaps and Ramsbottom 1966; Fricker 2000); and $\omega_n(t) = 2\pi f_n(t) = n2\pi f_1(t)$ is the angular frequency of the oscillator, here given an explicit time dependence to account for the seasonal variation in seiche frequency. For simplicity, we take γ to be a constant, though theories find it depends on amplitude and period (e.g., the damping time T_d, Eq. 4). In Eq. 1, L and H are, respectively, the length and depth of the ideal basin; h_2 is the thickness of the lower stratified layer, equal to $H - h_1$, where h_1 is the thickness of the upper layer, and ρ_2 is the density of the lower layer. The term $\rho_a C_D {U_{10}}^2$ gives the surficial wind stress, where ρ_a is the atmospheric density and C_D is a drag coefficient that by convention is calibrated to the wind speed U_{10} measured 10 m above the surface. The time dependence of the drag coefficient C_D arises through its dependence on $U_{10}(t)$. The ad hoc parameter t_0 allows for a time difference between the measured wind speed and the response of the seiche. The cosine factor selects the component of the wind stress parallel to the long axis of the lake where θ is the measured wind-bearing relative to north, and φ adjusts for the orientation of the lake's long axis relative to north, which we estimate to be $-20.0°$ and $-7.8°$ for Owasco and Seneca Lakes, respectively.

Theory: Fitting the damped-oscillator parameters

To estimate the damped-oscillator parameters γ and $\omega_1(t)$, a function $\mathcal{F}(t)$ was designed to fit the filtered thermocline depth $h_{LP}(t)$ using a nonlinear least-squares fitting algorithm. Because $h_{LP}(t) = h_{1qs}(t) + \delta h_{LP}(t)$, $\mathcal{F}(t)$ was constructed with two terms: one for the slowly varying quasi-static depth of the thermocline $h_{1qs}(t)$, which we represent with a polynomial $P_{qs}(t)$, and the second for the H1 internal-seiche oscillations $\delta h_{LP}(t)$, represented by a Green's function convolution giving a particular solution to the damped oscillator of Eq. 1:

$$\mathcal{F}(t) = P_{qs}(t) + \mathcal{A}\frac{4h_2}{\rho_2 LH}\int_{t-T}^{t} C_D(t'-t_0)\rho_a U_{10}^2(t'-t_0)G_1(t,t')dt' \tag{2}$$

Here, $G_1(t,t')$ is the Green's function, and $\mathcal{A}$ is an amplitude introduced to accommodate differences between the idealized model and the actual basin, as well as to accommodate the fact that $\delta h_{LP}(t)$, being measured at a field station, has a smaller value than if it were measured at the basin endwall to which Eq. 1 pertains. To our knowledge, Green's function for a damped oscillator with a slowly varying natural frequency is unavailable, so we derive it (Supporting Information, Variable frequency Green's Function) with the result:

$$G_n(t,t') = \frac{e^{-\gamma(t-t')}}{\left(\omega_n^2(t)-\gamma^2\right)^{1/4}\left(\omega_n^2(t')-\gamma^2\right)^{1/4}} \sin\int_{t'}^{t}\sqrt{\omega_n^2(t'')-\gamma^2}dt'' \tag{3}$$

Note that the lower time-limit of the convolution in Eq. 2 is formally negative infinity, which in practice we replace with a time preceding t by T (8 d for Owasco Lake, and 11 d for Seneca Lake) which the exponential decay in Green's function (Eq. 3) allows to high accuracy.

In Eq. 2, we take the length L to be the "baroclinic length," that is, the horizontal distance along the thalweg between the points where the horizontal thermocline meets the lake bed (Stevens and Lawrence 1997; Simpson et al. 2011; Dorostkar and Boegman 2013). For simplicity, the thermocline is fixed at its depth averaged over the stratified season: 13.2 m for Owasco Lake, and 15.3 m for Seneca Lake. Similarly, H is taken to be the mean lake-depth along the thalweg between the baroclinic endpoints (Lemmin and Mortimer 1986). In determining L and H for Seneca Lake, we use the bathymetry of Mullins et al. (1996); for Owasco Lake, we employ FLI's more detailed bathymetry (J. D. Halfman, unpubl.). The resulting baroclinic L and H for Owasco Lake are 16.0 km and 40.1 m, respectively, and for Seneca Lake, 53.7 km and 140.0 m.

The fitting parameters in $\mathcal{F}(t)$ comprise: (i) the coefficients of the third-order polynomial $P_{qs}(t)$ that approximates the slowly varying depth h_1, and hence also gives h_2 in Eq. 2 via $H - h_1$; (ii) the amplitude $\mathcal{A}$; (iii) the damping coefficient γ, taken to be constant; (iv) the coefficients of a 3rd- or 5th-order polynomial representing the varying H1-mode frequency $f_1(t) = \omega_1(t)/2\pi$; and (v) the time t_0 that allows for a time difference between the application of stress and the internal-seiche response. The methods used to obtain the initial trial coefficients of the polynomials $P_{qs}(t)$ and $f_1(t)$ used for fitting are detailed in Supporting Information, Initial Values, and Fig. S3.

Once a fit converges, $\mathcal{F}(t)$ represents with $P_{qs}(t) + \mathcal{A}\zeta_1(t)$ the best estimate of the data-derived thermocline depth $h_{LP}(t) = h_{1qs}(t) + \delta h_{LP}(t)$. To obtain the internal-seiche waveform itself, the fitted polynomial $P_{qs}(t)$ is subtracted from both $\mathcal{F}(t)$ and $h_{LP}(t)$ in order to obtain the fitted damped-oscillator waveform $\mathcal{A}\zeta_1(t) = \mathcal{F}(t) - P_{qs}(t)$ and the data-derived waveform $\delta h_{LP}(t) = h_{LP}(t) - P_{qs}(t)$. The waveforms can then be compared directly, as is done later in this paper (Fig. 2b,d for Owasco Lake; Fig. 2f for Seneca). Finally, the time series $\delta h(t)$ for the unfiltered data-derived internal-wave, which includes NLIWs, is computed via $\delta h(t) = h(t) - P_{qs}(t)$.

Theory: Internal seiche degeneration times

At small amplitudes, the internal seiche is expected to lose energy mainly through viscous friction between seiche-induced currents and the lakebed (Heaps and Ramsbottom 1966; Spigel and Imberger 1980; Fricker and Nepf 2000; Gloor et al. 2000).

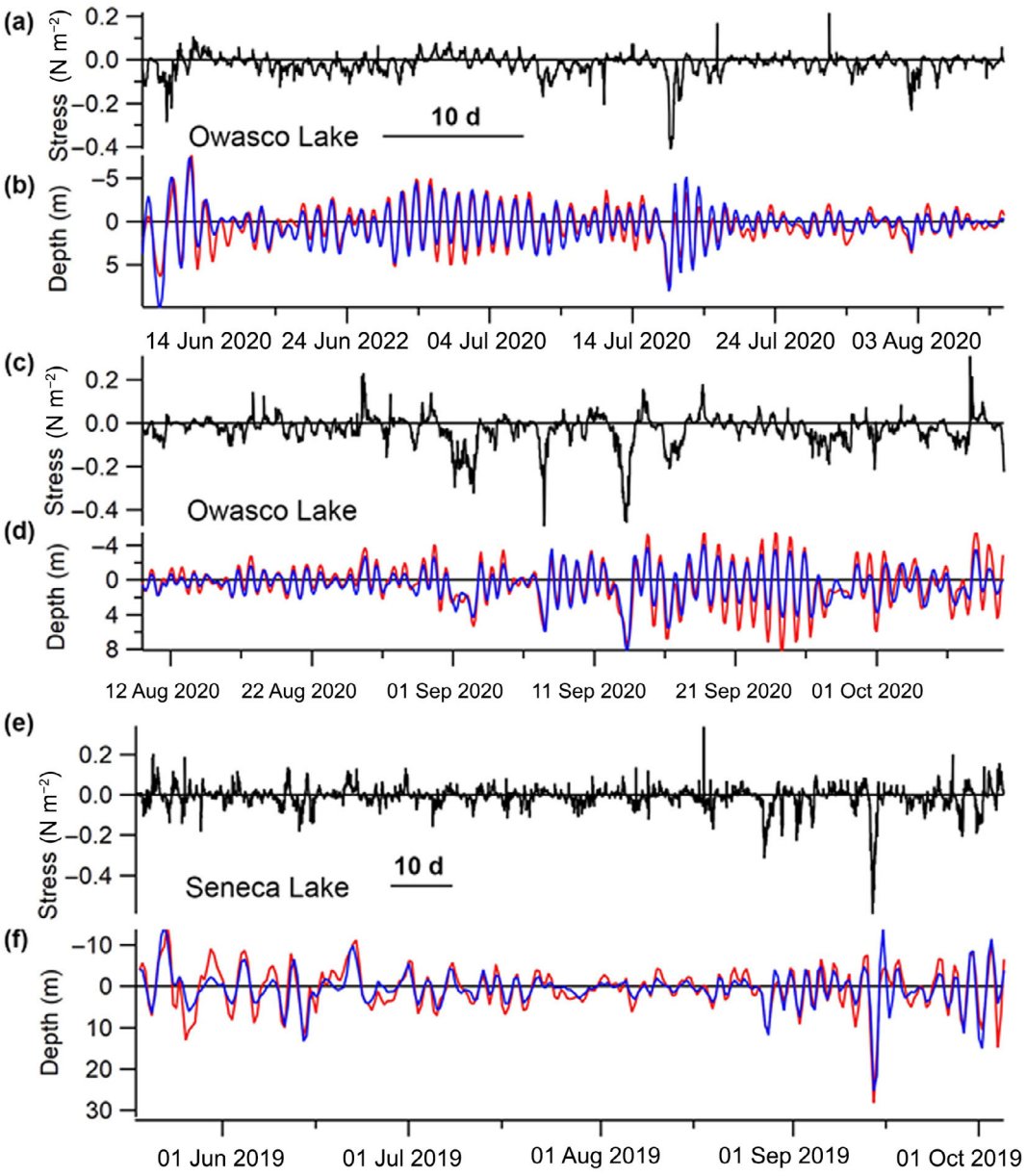

Fig. 2. Fitting results for Owasco and Seneca Lakes. (**a**,**c**,**e**) Wind-stress parallel to the lakes' axes; northerly winds are positive. (**b**,**d**,**f**) Data-derived approximation to the H1 internal-seiche displacement $\delta h_{\mathrm{LP}}(t)$ (red traces) compared to the fitted damped-oscillator displacment $\mathcal{A}\zeta_1(t)$ (blue traces). Displacement is plotted as depth relative to the quasi-static thermocline depth $h_{1\mathrm{qs}}$ (positive values indicate greater depth).

At often encountered larger amplitudes, however, loss is dominated through degeneration into various NLIW modes. The presence of these modes leads to a propagating basin-scale nonlinear wave—the "surge"—that is bounded by a steep slope in the thermocline (Horn et al. 2002; Boegman et al. 2005) that we call a "front." Degeneration to surges will dominate loss if their formation time, that is, the steepening time T_s (Hunkins and Fliegel 1973; Farmer 1978; Horn et al. 1986), is less than a characteristic viscous-loss damping time T_d. These times may be estimated via Eqs. 4 and 5, obtained in the Supporting Information, Internal Seiche Degradation, from formulas compiled in a seminal paper by Horn et al. (2001) and listed in Supporting Information Table S3.

$$T_d = \frac{236 h_2 H \sqrt{\nu P}}{eL} \frac{P}{\eta_0} \tag{4}$$

$$T_s = \frac{h_1 h_2}{3|(h_1 - h_2)|} \frac{P}{\eta_0} \tag{5}$$

Here, P is the period of the H1 internal seiche; e is the bottom roughness, assumed to be 0.06 m; ν is the kinematic viscosity

of the bottom layer, assumed to be the viscosity at 6°C, or 1.27×10^{-6} m^2 s^{-1}; h_1 and h_2 are, respectively, the thicknesses of the upper and lower layers; $H = h_1 + h_2$ is the basin depth; L is the basin length; and η_0 is the internal seiche amplitude (sum of all Hn modes) at a basin endwall. Eqs. 4 and 5 pertain to the idealized two-layer model of a rectangular basin subjected to the sudden onset of a constant and uniform wind lasting longer than $P/4$. At $P/4$, the thermocline assumes a tilted planar form about which, if losses are small, it undulates with amplitude η_0 at an endwall due to the superposition of all odd Hn modes (Heaps and Ramsbottom 1966; Spigel and Imberger 1980). To compute the times T_d and T_s, we evaluate η_0 as a time series from selected peaks and valleys of the estimated H1 oscillations $\delta h_{LP}(t)$, as detailed in the Supporting Information, Data Processing. Using the times t_p in the series, we then construct series for T_d and T_s using Eqs. 4 and 5, where the thermocline depth h_1 is set to $P_{qs}(t_p)$, the polynomial-fitted depth of $h_{1qs}(t)$. Similarly, the period P is computed at t_p from the polynomial-fitted seiche frequency $f_1(t)$.

We note in passing that Eqs. 4 and 5, both being proportional to $(\eta_0)^{-1}$, are unable to predict from the condition $T_d < T_s$ a threshold amplitude for η_0 below which loss to surges is unimportant. Such a threshold can be found for a laboratory tank (Horn et al. 2001; Stashchuk et al. 2005) because the two-layer model yields a different expression for T_d. Hence, Eq. 4 for T_d specific to a lake (Spigel and Imberger 1980) must be regarded as an indicative approximation that oversimplifies the complex process of viscous damping (Fricker and Nepf 2000; Gloor et al. 2000).

An internal seiche may also degenerate into nonlinear bores and Kelvin–Helmholtz billows which arise at the thermocline due to supercritical current-shear between the upper and lower layers. We evaluate the likelihood of these modes occurring in Supporting Information, Internal Seiche Degradation, again using formulas for the mode formation-times based on the two-layer model (Horn et al. 2001) as listed in Supporting Information Table S3. The results, presented in Supporting Information Fig. S4, indicate that these modes occur infrequently if at all in Owasco Lake, but likely several times a season in Seneca Lake.

Results

Damped-oscillator fitting

The damped-oscillator fits and the driving wind stresses for Owasco and Seneca Lakes are shown in Fig. 2. Winds from the north are positive to be properly phased to seiches measured at the northern ends of the lakes. Owasco Lake's horizontal scale is extended to better show details since its seiche undulates ~ 3 times faster than Seneca's, due largely to its shorter length as predicted by the modified Merian equation (Supporting Information Eq. S8). For Seneca Lake, we focus on the FLI station because, being near an endwall, it requires only a small extrapolation to determine the endwall amplitude η_0 (unlike the GLERL station), and because the instantaneous thermocline remained well above its deepest temperature sensor at all times (unlike the USGS station). The other two stations on Seneca Lake gave comparable fits and similar values for the key fitting parameters (Table 2). Despite the simplicity of the damped-oscillator model, the fits in Fig. 2 pick up nearly every feature of the internal seiche displacements, and reasonably match relative amplitudes. The tendency to underestimate the absolute amplitude may be due to circulating surges for which the damped-oscillator model does not account (*see* Discussion).

As fitted, the amplitude $\mathcal{A}$ ideally equals the ratio of the H1-mode displacement at the field station to its displacement at the baroclinic endwall, a distance d away. Scaling by the $\cos(\pi x/L)$ dependence of an ideal H1 mode, the endwall amplitude is $\mathcal{A}/\cos(\pi d/L)$. The values (Table 2) are gratifyingly close to the ideal value of unity, considering the simplicity of our damped-oscillator paradigm and the two-layer model on which it is based.

Our model's simplicity may be responsible for the negative sign of the offset t_0, which implies that the damped-oscillator analog lags the response of the actual seiche to the wind stress. While the offset is small, amounting to ~ 6% of a period for Owasco Lake, and ~ 10% for Seneca Lake, it appears to be a characteristic of our model because all fits, for all stations, exhibited the same sign for t_0.

Internal seiche resonances

For Owasco Lake, two separate periods of wind-driven resonance are suggested by the strong and regular undulations of the thermocline in response to a modest diel wind-stress around 01 July (Fig. 2b) and 24 September (Fig. 2d). Resonant behavior is confirmed by the spectrograms in Fig. 3a,b. Both the wind stress and the responding thermocline undulations $\delta h(t)$ exhibit consistent spectral intensity at 1 cpd, but the intensity for the undulations becomes pronounced both times the seiche natural-frequency $f_1(t)$ passes through 1 cpd, indicative of resonance. (Strong vertical bands denote storm events.) Note that the intensified resonant-segments when $f_1(t)$ crosses 1 cpd are mirrored by distinct bands at the second harmonic, a likely consequence of surges (*see* Discussion).

Table 2. Fitting results for selected parameters.

Parameter	Seneca*	Owasco
$\mathcal{A}/\cos(\pi d/L)$†	0.59 to 0.85	0.68
τA (d)‡	2.0 to 2.3	1.8
P_{min} (d)$	2.1 to 2.3	0.77
$t0$ (hr)	−6.5 to −5.0	−1.6

*Numbers span the range of values returned by the fitting for the three Seneca Lake stations.
†Dimensionless H1 amplitude at the baroclinic endwall located a distance d from the field station; ideal value is unity.
‡Amplitude decay time.
$Minimum H1 period.

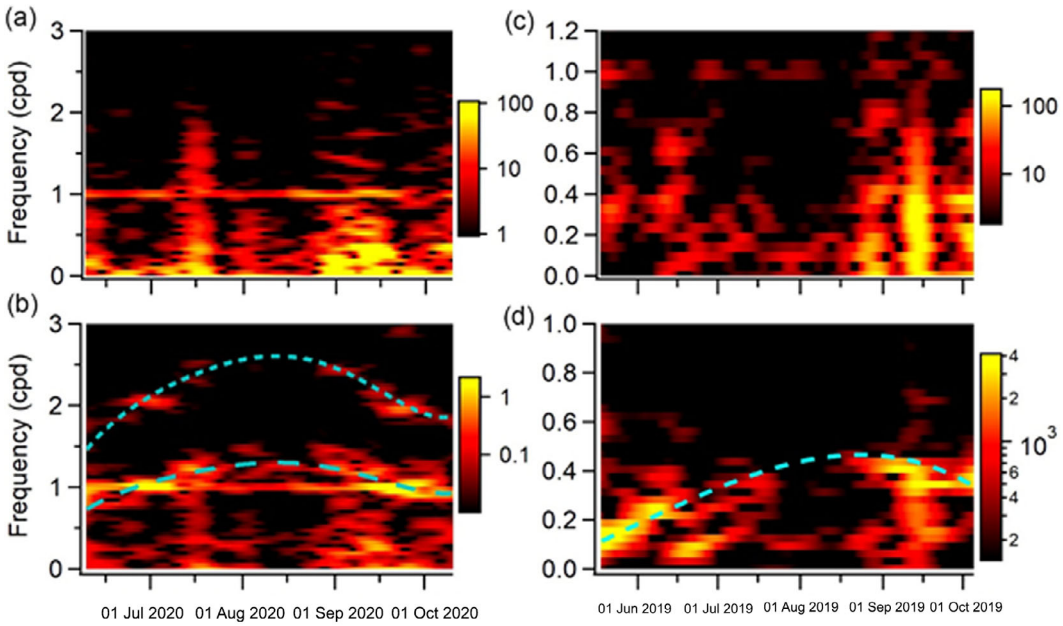

Fig. 3. Spectrograms of the wind stress (top panes) and internal-wave undulations $\delta h(t)$ (bottom panes) for Owasco Lake (left panes) and Seneca Lake (right panes). The long-dashed curves plot the fitted natural-frequency $f_1(t)$ of the damped oscillator. The short-dashed curve of (**b**) plots $2f_1(t)$ to locate where second-harmonic contributions would occur. The frequency axis of (**c**) extends beyond the Nyquist limit of (**d**) to show the diel wind pattern. The spectral intensities (arb. units) are independently scaled to be most informative. Spectrograms were computed through the short-time Fourier transform using a Hanning filter applied to waveform-segments of $\pm$ 10.7 d around each date/time for the wind stress, and $\pm$ 16 d for the internal waves.

Further support for resonance is provided by the evolution of the phase shift between the oscillations of the wind stress and those of the seiche displacement (Fig. 4a). Notations above the traces qualitatively relate the well-known phase lag of a damped-oscillator's displacement relative to a sinusoidal driving force, given by $\tan\varphi_{\text{lag}} = 2\omega\gamma/(\omega_1^2 - \omega^2)$ (Thornton and Marion 2008), where ω is the driving angular-frequency, and ω_1 the oscillator's natural frequency. Although the expression for φ_{lag} pertains to steady state, we employ it in the spirit of the quasi-steady-state conditions that apply here, that is, $\dot{\omega}_1(t) \ll \omega_1(t)\gamma$. The shifting phase as the seiche frequency passes through resonance is quantitatively accounted for by Green's function fit (blue trace in Fig. 4b), which overlaps well the seiche displacements (red trace).

While Owasco Lake reliably resonates with the diel wind frequency twice each season (the 2019 season exhibited resonant behavior very similar to 2020), Seneca Lake requires a fortuitous series of wind events near its $\sim$ 2-d period to build up a resonant response. Such a series occurred over 10 d in 2019 beginning on 27 August that led to the strong and regular oscillations centered around 02 September in Fig. 2f. Resonant spectral intensity is also evident in the spectrogram of Fig. 3d, though it is overshadowed by the following intense storm event around 14 September.

Surge influences on damping and waveforms

The endwall amplitudes η_0 used to compute the damping times through Eqs. 4 and 5 are plotted in Fig. 5a,c. The tendency for larger amplitudes to occur in early and late season when stratification is weaker is typical (Lemmin 1987; Arnon et al. 2019), though for Owasco Lake the two intervals of resonance also contribute. In the bottom panels, the computed damping times are compared to the fitted amplitude decay-time $\tau_A = 1/\gamma$ (horizontal dashed lines). That τ_A is commensurate with the surge steepening time T_s for both lakes is a key finding, and indicates that the seiche degrades largely into surges. Note that damping times depend on seasonally varying parameters as well as seiche amplitude (e.g., Eqs. 4, 5), whereas for practical reasons our fitting algorithm assumes a constant damping time τ_A. Hence our fitted values for τ_A must be considered an approximate seasonal average.

Further evidence for the presence of surges is provided by the waveforms of the thermocline displacement for both lakes. Seneca Lake's surges produce conspicuous steep plunges in $h(t)$ resolved at both the USGS and GLERL stations (Fig. 6). The timing of the surge-fronts at the two stations permits constructing the trajectory of a bidirectionally propagating surge. In Fig. 6d, crosses are plotted with abscissas at the time a surge front passed either the GLERL or USGS station, and ordinates at the corresponding location of each station expressed as a fraction of the baroclinic length from the south endwall, 0.37 for the GLERL station, and 0.97 for the USGS station. A positive-slope trajectory-segment connects successive crosses, and is then extrapolated back and forward to the $y = 0$ and $y = 1$ gridlines representing the southern and northern endwalls. The negative-slope segment connects the $y = 1$

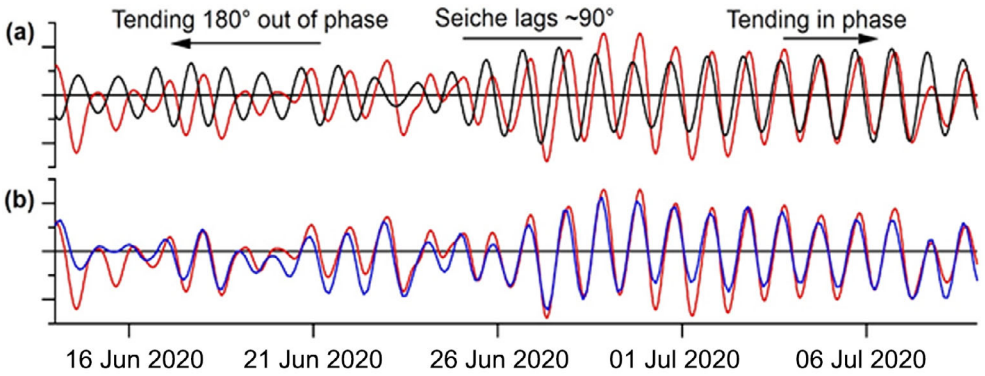

Fig. 4. Phase relationships during Owasco's early-season resonance. Units are arbitrary as amplitudes have been adjusted to aid comparisons. (**a**) Comparison of the diel component of the wind stress (black) to the low-pass-filtered internal-seiche displacement $\delta h_{LP}(\boldsymbol{t})$ (red). Labels note the phase relation expected between the driving force and the displacement of a damped oscillator as its natural frequency varies. (**b**) $\delta h_{LP}(t)$ (red) compared to the fitted damped-oscillator response (blue), which successfully unwinds the phase.

gridline-intercept to the next GLERL cross, and is then extrapolated forward to $y = 0$ (i.e., the x-axis). The segments should meet at the x-axis if they trace a surge initiated in phase with the seiche, or reflected back and forth between the endwalls, or a combination of both. (As a basin-scale wave, the surge is expected to exhibit significant reflection; Horn et al. 2002). This is the case: the first five near-meetings on the x-axis are separated by an average of only 53 ± 120 min, amounting to less than 2% of the seiche period, and consistent with zero. (The last near-meeting is omitted because a new wind event is beginning to reset the system.)

In contrast to Seneca Lake, the surges in Owasco Lake manifest as a weaker sawtooth-like asymmetry in the thermocline displacements (Fig. 7). The waveform is attributable to surges through its similarity to the waveforms reported for the stratified-interface in laboratory tanks driven into the surge regime (Boegman et al. 2005; Boegman and Ivey 2012; *see* Discussion). In addition, there is a strong correspondence between the frequency-filtered components of the waveform in Fig. 7b and those of the tank interface waveform (*see* Discussion). The contribution of surges to the internal-seiche waveform in Owasco Lake is further clarified by the sawtooth difference-curve obtained by subtracting the fitted seiche waveform $\mathcal{F}(t)$ from the instantaneous thermocline displacement $h(t)$ (Fig. 7d and Discussion).

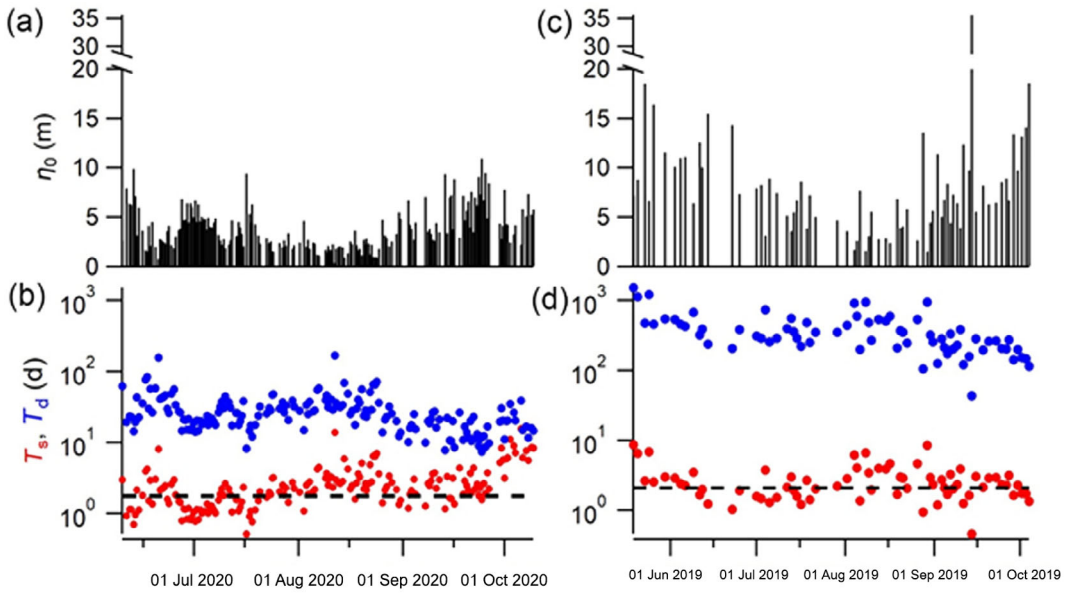

Fig. 5. Internal-seiche endwall amplitudes η_0 for (**a**) Owasco and (**c**) Seneca Lakes. Computed viscous decay-times T_d (blue) and surge formation times T_s (red) for (**b**) Owasco and (**d**) Seneca Lakes. The fitted values for the amplitude decay time τ_A are plotted as dashed lines.

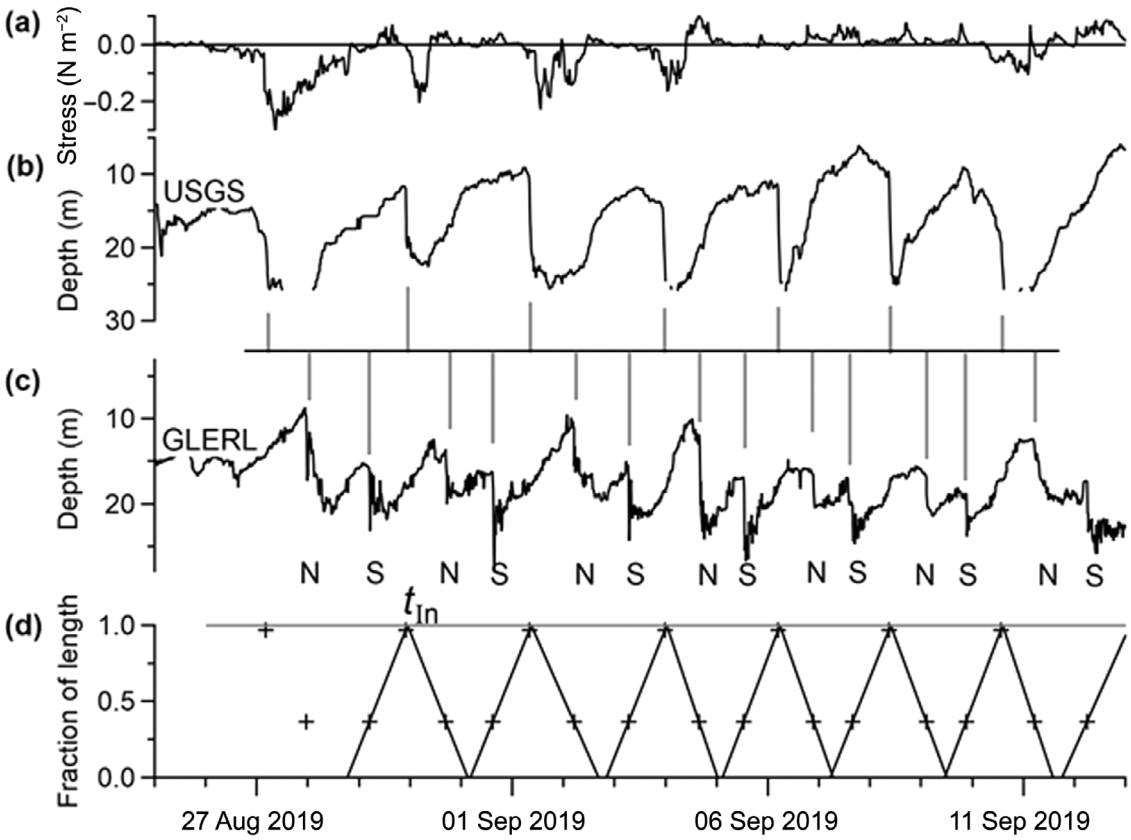

Fig. 6. Effect of surges in Seneca Lake during a period when four wind-events resonantly pumped the internal seiche. Gray vertical lines mark surge fronts. (**a**) Wind stress; north winds are positive. (**b**,**c**) thermocline depth $h(t)$; (**d**) Constructed surge-front trajectory. The times t_{In} denote when the trajectory intersects $y = 1$ as used in the analysis. *N* and *S* label fronts passing the GLERL station from the north or the south.

Discussion

Damped-oscillator behavior

Our damped-oscillator model reasonably reproduces the H1 undulations in the thermocline pumped by variable winds, despite the presence of circulating surges (Fig. 2). Thus, the model accommodates three well-known damped-oscillator responses, as best exemplified by Owasco Lake, namely (i) impulsive, (ii) steady state, and (iii) resonant, the latter two being consequences of seiche's $\sim$1-cpd natural frequency lying near the diel wind frequency. The steady state aspect is shown by the marked response at 1 cpd across the full-season spectrogram of the internal-wave undulations in Owasco Lake (Fig. 3b), which reflects the fact that a damped oscillator driven at a constant frequency responds at the same frequency (with a phase shift) independent of its natural frequency. Since the wind is not perfectly regular, the seiche at times also exhibits responses near the frequency associated with impulsive excitation, namely $f_\gamma = \sqrt{\omega_1^2 - \gamma^2}/(2\pi)$ (Thornton and Marion 2008). The shift $f_1 - f_\gamma$ from the natural frequency f_1 is small: using fitted values from Table 2, the damping adjustment to f_1 is less than 2% for both lakes. Patches of enhanced spectral density in Fig. 3b indeed overlap the fitted arc of $f_1(t)$ (long-dashed curve) during the storm events in mid-July and the first half of September. An impulsive response is also apparent in Owasco's seiche waveform itself early in the season (Fig. 2b), when the waveform clearly undulates more slowly than 1 cpd up to $\sim$14 June 2020 in response to strong wind events.

The spectrogram for Seneca Lake also shows an impulsive response to wind frequencies near its natural frequency (Fig. 3d), most pronounced early in the season and during the storm event in mid-September (Fig. 3c). In contrast to Owasco Lake, however, the Seneca Lake seiche, owing to its lower natural frequency ($f_1 \lesssim 0.4$cpd), responds negligibly to the diel wind frequency (Fig. 3c), as confirmed by Fourier analysis of $\delta h(t)$ measured at the USGS station (not shown). The 12-h cycle of the FLI station, being at the Nyquist frequency of 1 cpd, would make any response at this frequency difficult to discern in the spectrogram of Fig. 3d.

The third oscillator response, resonance, can be induced if a series of wind pulses fortuitously repeats near the seiche natural frequency, as occurred in Seneca Lake in Fig. 6, and has been suggested for the H1 mode in Cayuga Lake ($\sim$2.4-d period; Henson 1959). However, resonance is best studied

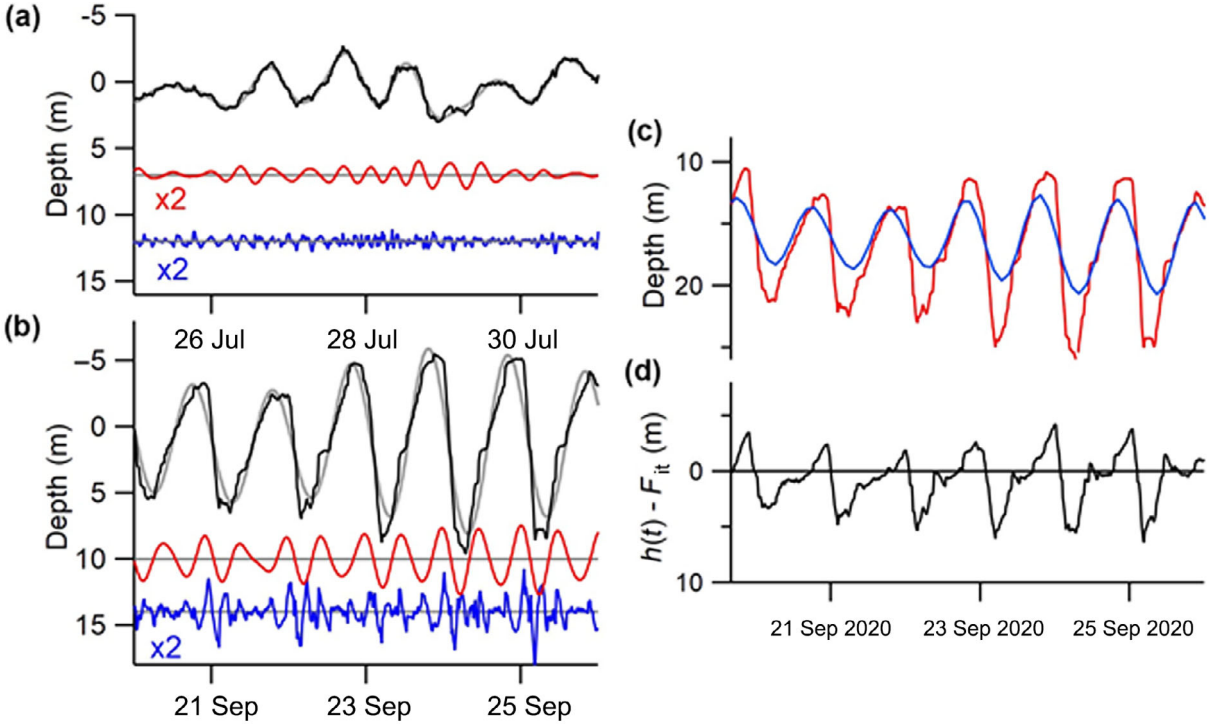

Fig. 7. Left panel: thermocline undulations $\delta h(t)$ (black) and three filtered components in Owasco Lake: (i) near the H1 frequency f_1 (gray; $f < 1.5f_1$); (ii) the second harmonic (red; $1.5f_1 < f < 3\ f_1$); (iii) higher frequencies (blue; $f > 3\ f_1$). Red and blue traces are offset from zero and multiplied by two ($\times$ 2) when needed for clarity. (**a**) A period of weaker winds and stronger stratification with $f_1 = 1.3$ cpd; (**b**) interval during the second resonance with $f_1 = 1$ cpd. (**c**) Thermocline depth $h(t)$ (red) and the corresponding damped-oscillator fit (blue) during Owasco Lake's second resonance. (**d**) Surge waveform (black) obtained by subtracting the fit from $h(t)$.

with the sustained driving force of a daily wind pattern. Internal-wave resonances at 1 cpd have been convincingly reported for Kelvin waves circulating around lakes with dimensions exceeding the Rossby radius (Antenucci and Imberger 2003; Gómez-Giraldo et al. 2006; Rozas et al. 2014). In Kinneret Lake, the Kelvin wave's seasonally varying frequency comes into resonance with the diel wind-frequency twice each season, much like Owasco Lake's H1 mode (Antenucci and Imberger 2003). Vertical mode wind-driven resonances have also been predicted (Ulloa et al. 2020) and observed (Münnich et al. 1992; Vidal and Casamitjana 2008; Pannard et al. 2011). Clear evidence for resonance of the H1 mode in elongated lakes seems more elusive. A parametric resonance has been suggested for Loch Ness (Thorpe 1974), and, more clearly, a near-resonance has been implicated in Lake Windermere (Woolway and Simpson 2017). Owasco Lake represents perhaps the clearest demonstration of resonance in the H1 mode for an elongated lake: during two distinct periods when the mode's natural-frequency passed through the diel wind frequency, the seiche exhibited (i) strong and regular oscillations (Fig. 2); (ii) enhanced spectral intensity at 1 cpd (Fig. 3b); and (iii) the expected change of phase with respect to the wind (Fig. 4). However, the resonant enhancement of amplitude is weaker than theory predicts (Thornton and Marion 2008). The weakened response may be attributable in part to an imperfect regularity of the wind stress, but more importantly to nonlinear degradation of the seiche energy into surges (Horn et al. 2001; Boegman et al. 2005; Boegman and Ivey 2012). In particular, wave-tank experiments show that degeneration into surges strongly stem the resonant enhancement of seiche amplitude (Boegman and Ivey 2012, fig. 10).

Internal seiche damping

The model returned amplitude decay-times τ_A matching the computed surge formation times T_s for both Owasco and Seneca Lakes (Fig. 5b,d). This finding is consistent with a report that the linear analytical theory of a driven damped-oscillator describes damping times of internal waves in a wave tank when degeneration into surges dominates (Boegman and Ivey 2012). Our finding that $\tau_A \approx T_s$, coupled with a report that the formula for T_s (Eq. 5) accurately describes surge formation times in a tank (Boegman et al. 2005), extends the applicability of the formula for T_s from tanks to elongated lakes, and indicates that the seiche in these lakes decay primarily to surges.

Using the fitted values from Table 2, $P/\tau_A \approx 1$ for Seneca Lake and $P/\tau_A \approx 0.4$ for Owasco Lake. Comparably rapid decays are listed in a compilation of field-derived damping times (Imam et al. 2013*b*), where the two longest elongated lakes have $P/\tau_A \sim 1$, and both exhibit surges (Horn et al. 1986;

Stevens et al. 1996). Likewise, tank experiments find that large-amplitude internal seiches can decay via surges as quickly as one seiche period (Boegman et al. 2005, fig. 7d). That Seneca Lake's value for P/τ_A is larger than Owasco's is attributable to its greater inherent nonlinearity as expressed by the nonlinear parameter $\varepsilon = (3/2)\eta_0 |h_1 - h_2| / (h_1 h_2)$, equal to the ratio of the nonlinear-to-linear coefficients in the Korteweg de Vries equation when it is derived within the two-layer model (Boegman et al. 2005). Evaluating the formula for ε using the seasonal means for h_1, the baroclinic lake depths H, and the values for η_0 plotted in Fig. 5a,c, we find the median value of ε for Seneca Lake is $\sim$2.7 times that of Owasco's. This is consistent with an independent field-assessment of ε: Through the formulas in Supporting Information Table S3, it can be shown that $\varepsilon = \frac{1}{2}P/T_s$, or, since we find that $\tau_A \approx T_s$, $\varepsilon \approx \frac{1}{2}P/\tau_A$. Using values from Table 2, we find P/τ_A for Seneca Lake is $\sim$2.5 times greater than Owasco.

Surge influences on internal-wave waveforms

The steep surge fronts in Seneca Lake (Fig. 6) occur at the USGS station once per H1 period, and twice per period at the GLERL station. The latter waveform (Fig. 6c) resembles that of a stratified interface measured with a sensor also removed from an endwall in a tank supporting counter-propagating surges (Boegman and Ivey 2012, fig. 1c). These plunges in both tank and lake are alternately separated by longer and shorter intervals, with the ratio of long to short intervals equal to the ratio of the distances from the sensor to the further and nearer ends of the basin. The timing is consistent with a surge propagating in both directions, and essentially phase locked to the internal seiche. This is verified by the constructed trajectory of Fig. 6d that follows the surge front propagating up and down Seneca Lake over a 2-week period. The finding that surges propagate in both directions augments an earlier report for Seneca Lake that reported surges and solitary wave-trains traveled only from south to north (Hunkins and Fliegel 1973). Bidirectional surges have also been documented in adjacent and comparably sized Cayuga Lake (Dorostkar and Boegman 2013).

Compared to Seneca Lake, the influence of surges in Owasco Lake is less pronounced, simply inducing an asymmetry to the waveform of thermocline undulations. For large excursions of the thermocline (Fig. 7b), the asymmetry bears a strong resemblance to the time-series of isotherm depths measured near either end of Baldeggersee Lake that were attributed to bidirectional surges (Lemmin 1987; see waveforms in this reference for Stas. 181 and 182 in figs. 4, 6). A comparable asymmetry is observed in the displacement of the interface between stratified layers in wave tanks with circulating surges (Boegman et al. 2005, fig. 5c–e; Boegman and Ivey 2012, fig. 1d). When the internal-seiche amplitude in Owasco Lake is smaller (Fig. 7a, black trace), the waveform asymmetry is reduced, though surges are still indicated by the presence higher frequency components (Fig. 7a, blue and red traces).

The similarity between seiche waveforms in a tank and Owasco Lake is tested more thoroughly by comparing waveform components after frequency filtering. In Fig. 7a,b, we applied low-pass, band-pass, and high-pass filters to the internal wave undulations $\delta h(t)$ with the same cutoff-frequencies relative to the H1 frequency f_1 as used in lab analyses (Boegman et al. 2005; Boegman and Ivey 2012). The decomposition in Fig. 7 resembles that presented by Boegman and Ivey (Boegman and Ivey 2012, fig. 1) by having a significant component at $2f_1$, consistent with the spectrogram of Fig. 3b. Also, the highest-frequency waveforms for both tank and lake (blue traces of Fig. 7a,b) exhibit bipolar spikes that are aligned with downward slopes of the $2f_1$ waveform, except here the spikes tend to occur on every other $2f_1$ oscillation rather than every oscillation as in the tank experiment. This occurs because the spikes arise from the front of the circulating surge, for which two are detected per seiche cycle at the tank sensor located 0.22 L from a tank endwall, but only one per cycle at the field station located 0.05 L from the baroclinic endwall, which is too close to resolve a new surge in the process of being formed or being a reflected. Other, high-frequency features in the blue traces of Fig. 7a,b may be a result of aliased sampling of the solitary-wave train that is resolved in the tank experiments.

The damped-oscillator fits for both lakes often underestimate the amplitude of the H1 mode (Fig. 2). The underestimate may be due to the surges, which, being synchronized to the seiche, contribute a Fourier component at f_1 to the waveform being fitted, $h_{LP}(t)$, that is not included in the damped-oscillator model. Assuming that the fit $\mathcal{F}(t)$ gives a reasonably good estimate of the H1 undulations, we examine the effect of surges on thermocline undulations by displaying the difference $\mathcal{S}(t) = h(t) - \mathcal{F}(t)$ for Owasco Lake in Fig. 7d. Because the system is nonlinear, $h(t)$ cannot be construed as a linear superposition of the seiche plus surge, but $\mathcal{S}(t)$ nevertheless permits visualizing the effect of high-frequency modes on the $h(t)$ waveform. In fact, the sawtooth waveform of $\mathcal{S}(t)$ in Fig. 7d is very similar to the pure seiche waveform measured at mid-tank in the lab where contributions from the H1 mode are absent (Boegman et al. 2005, fig. 6c,d; Boegman and Ivey 2012, fig. 1c). We deem this sawtooth-like influence of surges to be the principal source of the pronounced second-harmonic component during Owasco's two resonances (Fig. 3b and red traces in Fig. 7a,b), rather than direct excitation of the H2 harmonic.

Conclusions

We developed a simple damped-oscillator model that employs an original Green's function to successfully reproduce the irregular undulations of the fundamental (H1) internal-seiche caused by a constantly varying wind. The model was demonstrated on the elongated but dissimilarly sized Owasco and Seneca Lakes in central New York state. The model extracts

the seasonal changes in the internal-seiche frequency and the seiche's amplitude-decay-time, despite the simultaneous presence of nonlinear surges. The surges are obvious in Seneca Lake through pronounced plunges in the waveform of thermocline undulations, but only suggested in Owasco Lake by an asymmetric waveform. Surges were confirmed in Owasco Lake by comparing its waveform to results reported for a wave tank with circulating surges. Importantly, the internal-seiche decay times, though obtained with a linear model, correspond to the formation times of nonlinear surges computed for both lakes with a simple formula proven for wave tanks, thus extending laboratory results to the field. The results show that surges rapidly degrade internal wave energy, within about one internal-seiche period for Seneca Lake, and two for Owasco. We attribute the difference to Seneca Lake's greater inherent nonlinearity as computed with an established nonlinear parameter, which we showed can be field determined in lakes with surge-limited internal seiches through the ratio of the internal seiche period to the seiche decay time. The internal seiche in Owasco Lake exhibits especially well-defined resonances early and late each season when the evolving seiche natural-frequency matches the diel wind frequency, but loss to surges limits the expected resonant enhancement in seiche amplitude, again consistent with wave-tank experiments. Finally, the surge in Seneca Lake was found to travel bidirectionally, amending an oft-cited report of only unidirectional propagation.

Data availability statement

Data available on request from the authors

References

Antenucci, J. P., and J. Imberger. 2003. The seasonal evolution of wind/internal wave resonance in Lake Kinneret. Limnol. Oceanogr. **48**: 2055–2061. doi:10.4319/lo.2003.48.5.2055

Arnon, A., S. Brenner, J. S. Selker, I. Gertman, and N. G. Lensky. 2019. Seasonal dynamics of internal waves governed by stratification stability and wind: Analysis of high-resolution observations from the Dead Sea. Limnol. Oceanogr. **64**: 1864–1882. doi:10.1002/lno.11156

Birge, E. A., and C. Juday. 1914. A limnological study of the Finger Lakes of New York. Bull. Bur. Fish. **32**: 525–609.

Boegman, L. 2010. Currents in stratified water bodies 2: Internal waves. *In* G. E. Likens [ed.], Lake ecosystem ecology. Academic Press.

Boegman, L., and G. N. Ivey. 2012. The dynamics of internal wave resonance in periodically forced narrow basins. J. Geophys. Res. Oceans **117**: C11002. doi:10.1029/2012JC008134

Boegman, L., G. N. Ivey, and J. Imberger. 2005. The energetics of large-scale internal wave degeneration in lakes. J. Fluid Mech. **531**: 159–180. doi:10.1017/S0022112005003915

Dorostkar, A., and L. Boegman. 2013. Internal hydraulic jumps in a long narrow lake. Limnol. Oceanogr. **58**: 153–172. doi:10.4319/lo.2013.58.1.0153

Farmer, D. M. 1978. Observations of long nonlinear internal waves in a lake. J. Phys. Oceanogr. **8**: 63–73. doi:10.1175/1520-0485(1978)008<0063:OOLNIW>2.0.CO;2

Finger Lakes Institute. 2021*a*. Owasco Lake water quality buoy. Available from http://fli-data.hws.edu/buoy/

Finger Lakes Institute. 2021*b*. Seneca Lake Water quality buoy. Available from http://fli-data.hws.edu/buoy/

Fricker, P. D. 2000. The effect of stratification and bathymetry on internal seiche dynamics. Ph.D. thesis. Massachusetts Institute of Technology.

Fricker, P. D., and H. M. Nepf. 2000. Bathymetry, stratification, and internal seiche structure. J. Geophys. Res. Oceans **105**: 14237–14251. doi:10.1029/2000JC900060

Gelda, R. K., A. T. King, S. W. Effler, S. A. Schweitzer, and E. A. Cowen. 2015. Testing and application of a two-dimensional hydrothermal/transport model for a long, deep, and narrow lake with moderate Burger number. **5**: 387–402. doi:10.5268/IW-5.4.804

Gloor, M., A. Wüest, and D. M. Imboden. 2000. Dynamics of mixed bottom boundary layers and its implications for diapycnal transport in a stratified, natural water basin. J. Geophys. Res. Oceans **105**: 8629–8646. doi:10.1029/1999JC900303

Gómez-Giraldo, A., J. Imberger, and J. P. Antenucci. 2006. Spatial structure of the dominant basin-scale internal waves in Lake Kinneret. Limnol. Oceanogr. **51**: 229–246. doi:10.4319/lo.2006.51.1.0229

Heaps, N. S., and A. E. Ramsbottom. 1966. Wind effects on the water in a narrow two-layered lake. Philos. Trans. R. Soc. Lond. **259**: 391–430. doi:10.1098/rsta.1966.0021

Henson, E. B. 1959. Evidence of internal wave activity in Cayuga Lake, New York. Limnol. Oceanogr. **4**: 441–447. doi:10.4319/lo.1959.4.4.0441

Horn, D. A., J. Imberger, and G. N. Ivey. 2001. The degeneration of large-scale interfacial gravity waves in lakes. J. Fluid Mech. **434**: 181–207. doi:10.1017/S0022112001003536

Horn, D. A., J. Imberger, G. N. Ivey, and L. G. Redekopp. 2002. A weakly nonlinear model of long internal waves in closed basins. J. Fluid Mech. **467**: 269–287. doi:10.1017/S0022112002001362

Horn, W., C. H. Mortimer, and D. J. Schwab. 1986. Wind-induced internal seiches in Lake Zurich observed and modeled. Limnol. Oceanogr. **31**: 1232–1254. doi:10.4319/lo.1986.31.6.1232

Hunkins, K., and M. Fliegel. 1973. Internal undular surges in Seneca Lake: A natural occurrence of solitons. J. Geophys. Res. **78**: 539–548. doi:10.1029/JC078i003p00539

Imam, Y. E., B. Laval, R. Pieters, and G. Lawrence. 2013*b*. The strongly damped baroclinic response to wind in a multi-basin reservoir. Limnol. Oceanogr. **58**: 1243–1258. doi:10.4319/lo.2013.58.4.1243

Imam, Y. E., B. E. Laval, and G. A. Lawrence. 2013*a*. The baroclinic response to wind in a small two-basin lake. Aquat. Sci. **75**: 213–233. doi:10.1007/s00027-012-0268-1

Lemmin, U. 1987. The structure and dynamics of internal waves in Baldeggersee. Limnol. Oceanogr. **32**: 43–61. doi:10.4319/lo.1987.32.1.0043

Lemmin, U., and C. H. Mortimer. 1986. Tests of an extension to internal seiches of Defant's procedure for determination of surface seiche characteristics in real lakes. Limnol. Oceanogr. **31**: 1207–1231. doi:10.4319/lo.1986.31.6.1207

Maderich, V., I. Brovchenko, K. Terletska, and K. Hutter. 2012. Numerical simulations of the nonhydrostatic transformation of basin-scale internal gravity waves and wave-enhanced Meromixis in lakes, p. 193–276. *In* K. Hutter [ed.], Nonlinear internal waves in lakes. Springer.

Mortimer, C. H. 1974. Lake hydrodynamics. Int. Ver. Theor. Angew. Limnol. Mitteilungen **20**: 124–197. doi:10.1080/05384680.1974.11923886

Mullins, H. T., E. J. Hinchey, R. W. Wellner, D. B. Stephens, W. T. Anderson, T. R. Dwyer, and A. C. Hine. 1996. Seismic stratigraphy of the Finger Lakes: A continental record of Heinrich event H-1 and Laurentide ice sheet instability. *In* Subsurface geologic investigations of New York Finger Lakes: Implications for late Quaternary deglaciation and environmental change. Geological Society of America.

Münnich, M., A. Wüest, and D. M. Imboden. 1992. Observations of the second vertical mode of the internal seiche in an alpine lake. Limnol. Oceanogr. **37**: 1705–1719. doi:10.4319/lo.1992.37.8.1705

Pannard, A., B. E. Beisner, D. F. Bird, J. Braun, D. Planas, and M. Bormans. 2011. Recurrent internal waves in a small lake: Potential ecological consequences for metalimnetic phytoplankton populations. Limnol. Oceanogr. Fluids Environ. **1**: 91–109. doi:10.1215/21573698-1303296

Rozas, C., A. de la Fuente, H. Ulloa, P. Davies, and Y. Niño. 2014. Quantifying the effect of wind on internal wave resonance in Lake Villarrica. Chile. Environ. Fluid Mech. **14**: 849–871. doi:10.1007/s10652-013-9329-9

Simpson, J. H., P. J. Wiles, and B. J. Lincoln. 2011. Internal seiche modes and bottom boundary-layer dissipation in a temperate lake from acoustic measurements. Limnol. Oceanogr. **56**: 1893–1906. doi:10.4319/lo.2011.56.5.1893

Spigel, R. H., and J. Imberger. 1980. The classification of mixed-layer dynamics of lakes of small to medium size. J. Phys. Oceanogr. **10**: 1104–1121. doi:10.1175/1520-0485(1980)010<1104:TCOMLD>2.0.CO;2

Stashchuk, N., V. Vlasenko, and K. Hutter. 2005. Numerical modelling of disintegration of basin-scale internal waves in a tank filled with stratified water. Nonlinear Process. Geophys. **12**: 955–964. doi:10.5194/npg-12-955-2005

Stevens, C., G. Lawrence, P. Hamblin, and E. Carmack. 1996. Wind forcing of internal waves in a long narrow stratified lake. Dyn. Atmos. Oceans **24**: 41–50. doi:10.1016/0377-0265(95)00409-2

Stevens, C. L., and G. A. Lawrence. 1997. Estimation of wind-forced internal seiche amplitudes in lakes and reservoirs, with data from British Columbia, Canada. Aquat. Sci. **59**: 115–134. doi:10.1007/BF02523176

Thornton, S. T., and J. B. Marion. 2008. Classical dynamics of particles and systems, 5th ed. Centage Learning.

Thorpe, S. A. 1974. Near-resonant forcing in a shallow two-layer fluid: A model for the internal surge in loch ness? J. Fluid Mech. **63**: 509–527. doi:10.1017/S0022112074001753

Ulloa, H. N., G. Constantinescu, K. Chang, D. Horna-Munoz, O. Hames, and A. Wüest. 2020. Horizontal transport under wind-induced resonance in stratified waterbodies. Phys. Rev. Fluids **5**: 054503. doi:10.1103/PhysRevFluids.5.054503

USGS Owasco. 2021. Owasco Lake platform. USGS No. 425327076313601. Available from https://ny.water.usgs.gov/maps/habs/

USGS Seneca. 2021. Seneca Lake platform. USGS No. 425027076564401. Available from https://ny.water.usgs.gov/maps/habs/

Vidal, J., and X. Casamitjana. 2008. Forced resonant oscillations as a response to periodic winds in a stratified reservoir. J. Hydraul. Eng. **134**: 416–425. doi:10.1061/(ASCE)0733-9429(2008)134:4(416)

Woolway, R. I., and J. H. Simpson. 2017. Energy input and dissipation in a temperate lake during the spring transition. Ocean Dyn. **67**: 959–971. doi:10.1007/s10236-017-1072-1

Acknowledgments

We thank Eric Anderson for his thoughtful review of an early draft of the manuscript. The thoughtful comments of two anonymous reviewers and Leon Boegman significantly improved the final version. We are also grateful to the crew of the RV William Scandling for logistical support in Lake Seneca. Financial support for the FLI buoy and GLERL deployments was from the Andrew Mellon, Fred L. Emerson, and other anonymous Foundations, the Great Lakes Environmental Research Laboratory (GLERL) and Hobart and William Smith Colleges. This is GLERL contribution #2037.

Conflict of Interest

The authors declare no conflicts of interest.

Submitted 31 January 2023
Revised 23 January 2024
Accepted 03 February 2024

Editor-in-Chief: K. David Hambright

Supplementary material for:

Internal wave resonance, surges, and strong nonlinear damping differentiated in two elongated lakes with the aid of an original Green's function

James P. Long,[1] John D. Halfman,[2]* Nathan Hawley[3]
[1]Finger Lakes Institute, Hobart & William Smith Colleges, Geneva, NY, 14456, USA;
[2]Department of Geoscience and Environmental Studies Program, Hobart & William Smith Colleges, Geneva, NY, 14456, USA; [3]Great Lakes Environmental Research Laboratory, Ann Arbor, MI 48108, USA
**Corresponding author: halfman@hws.edu*

Table S1. List of Greek symbols.

α	Lowest order nonlinear coefficient in the Korteweg-deVries equation	κ	A constant used in deriving the Green's function $G_n(t,t')$
γ	Internal seiche amplitude-damping-coefficient	ν	Kinematic viscosity
δ_b	Thickness of the turbulent bottom boundary layer	ρ	Temperature-dependent water density
ε	Nonlinear parameter charactering the degree of internal-wave nonlinearity in a lake	$\rho(z,t)$	Density depth-profile at time t
$\delta h(t)$	Instantaneous thermocline displacement from equilibrium at a field station	ρ_a	Density of air
$\delta h_{LP}(t)$	Low-pass filtered version of $\delta h(t)$ approximating the H1 mode undulations	ρ_1, ρ_2	Respective densities of the upper and lower layers in the two-layer model
δ_p	Metalimnion thickness	τ_A	Fitted value for the 1/e decay time of the H1 internal seiche amplitude
$\zeta(t)$	A function representing the thermocline displacement in Heaps and Ramsbottom (1966)	φ	Angle of lake axis from north
$\zeta_n(t)$	Displacement of the nth damped oscillator, representing the displacement of the Hn mode at a basin endwall, obtainable in principle via Eq. S3, and in practice for the H1 mode via fitting with Eq. 2	$\phi(t)$	A phase function used in deriving the Green's function $G_n(t,t')$
ζ_{n0}	Maximum displacement of the nth damped oscillator, i.e., its amplitude of oscillation	φ_{lag}	Phase lag of a damped oscillator's displacement relative to a harmonic driving force
η_0	Thermocline displacement from equilibrium at a basin endwall due to superposition of all Hn modes	ω_n	Natural angular-frequency of the n^{th} damped oscillator, i.e. $2\pi f_n$
θ	Wind bearing relative to north	ω_γ	Damping-shifted angular frequency of a damped oscillator

Table S2. List of alphabetic symbols. Equation numbers in the Supplemental Information are prefixed with "S."			
A	H1 mode amplitude at a field station	$P_{qs}(t)$	Polynomial obtained by fitting that approximates h_{1qs}
$\mathcal{A}$	An amplitude included in $\mathcal{F}(t)$	$\mathcal{S}(t)$	$=h(t)-\mathcal{F}(t)$, effect of surges on H1 waveform
$a(t)$	An amplitude function used in deriving $G_n(t,t')$	t	Time
A_b	Basin bed area	$T(z, t)$	Temperature depth-profile at time t
c_0	Internal-wave phase velocity	t_0	Time offset used in fitting function $\mathcal{F}(t)$
C_D	Wind-surface drag coefficient	T	Time interval over which the Green's function is integrated
d	Distance from a field station to an endwall	T_b	Formation time for a bore
e	Basin bed roughness	T_d	Computed 1/e decay time of the H1-mode amplitude
f	Frequency	t_{In}	Time that an n^{th} surge arrives at the north end of Seneca Lake, relevant to Fig. 6
$\mathcal{F}(t)$	Function that fits the wind-driven damped-oscillator model to $h_{LP}(t)$	T_{KH}	Formation time for Kelvin-Helmholtz billows
$f_1(t)$	Seasonally varying natural frequency of the H1-mode internal seiche	T_s	Formation time of a surge
f_n	Natural frequency of the n^{th} damped oscillator	$T_{TC}(t)$	Quasi-static temperature of the thermocline
$f_{Mn}(t)$	Seasonally varying frequency of the mode Hn computed via Eq. S8	$U(t)$	Measured wind speed
f_γ	Damping-shifted frequency of a damped oscillator	U_1, U_2	The current velocities of the upper and lower layers, respectively
g'	Reduced gravitational constant	$U_{10}(t)$	Wind speed 10 m above lake surface
$G_n(t,t')$	Green's function for the n^{th} mode		
H	Depth of a basin. For a lake, the mean depth along baroclinic length L.	U_{max}	Maximum depth-averaged current used to compute viscous losses
$h(t)$	Instantaneous depth of the thermocline	V	Basin volume
$h'(t)$	Instantaneous depth of the thermocline obtained with Eq. S1. Used to derive $h(t)$	W	Basin width
$h'_{qs}(t)$	Quasi-static depth of thermocline inferred from Eq. S1. Used to derive $h(t)$	x	Coordinate along the lake thalweg
h_1, h_2	Respective thicknesses of upper and lower layers in the two-layer model	y	Distance along thalweg in units of L, relevant to Fig. 6
$h_{1qs}(t)$	Quasistatic depth of the thermocline	y_1, y_2	Homogeneous solutions to the damped-oscillator differential equation used to derive $G_n(t,t')$
$h_{LP}(t)$	Low-pass filtered version of $h(t)$ to isolate the H1-mode contribution to the instantaneous thermocline depth	z	Depth measured from surface
Hn	Designation for the n^{th} horizontal mode	z_0	Water surface-roughness parameter
L	Baroclinic length of the basin	$\mathcal{Z}(t)$	Instantaneous depth where $T_{TC}(t)$ is found
P	Period of the H1 internal seiche mode		

Data processing

Fundamental to the analysis in the main text is the determination of the time varying depth $h(t)$ of the thermocline at a given field station. The thermocline depth was extracted from the measured time-series of a temperature profile, $T(z,t)$, in two stages, which are explained with the aid of Fig. S1, using Owasco Lake as an example. In the first stage (Fig. S1a), we find an approximation $h'(t)$ to $h(t)$ via the first moment of the gradient in density ρ(z,t) (Patterson et al. 1984; Stevens et al. 1996; Cossu and Wells 2013):

$$h'(t) = \frac{\int_o^H z \frac{\partial \rho(z,t)}{\partial z} dz}{\rho(H,t) - \rho(0,t)}, \tag{S1}$$

where z is depth measured from the surface (positive downward), and H is the mean depth along the so called baroclinic length L (as defined in the main text following Eq. 3). The density profile at time t, $\rho(z, t)$, is obtained from the measured temperature-profile by converting temperature to density with Kell's formulation (Jones and Harris 1992). The influence of dissolved solids on density was neglected since it would increase the thermally induced density difference from surface to bottom by at most one percent. In practice, for depths greater than the deepest temperature sensor employed, we fix ρ(z, t) to the density at that deepest sensor. Because we also fix the temperature between the upper sensor and the surface to be that of the upper sensor, the integral in Eq. S1 can give inaccurate results if that sensor becomes too deep. Such is the case for several strong wind events that swayed the upper sensor on the GLERL mooring in Seneca Lake to depths up to 5 m deeper than its nominal 2.5-m depth. This led to a waveform $h'_{LP}(t)$, the low-pass filtered version of $h'(t)$, that could not be fit by the damped-oscillator fitting algorithm. Hence, we devised an approach more local in z for finding $h(t)$, as explained next.

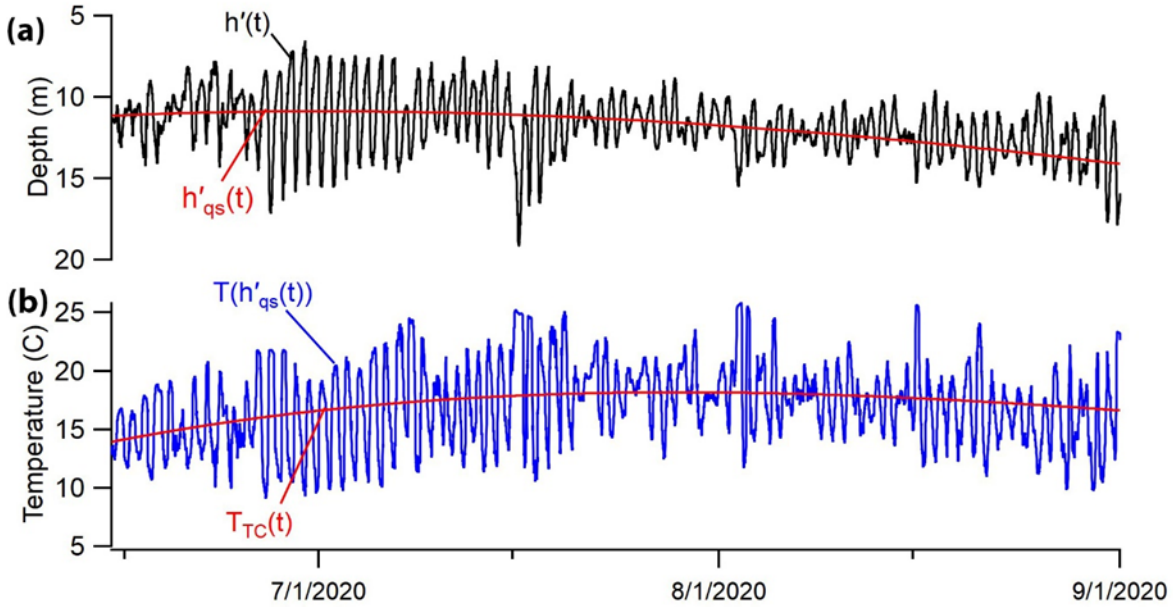

Fig. S1 *Steps to determine the instantaneous thermocline depth h(t), using Owasco Lake as an example. Later dates are omitted for clarity. (a) h'(t) via Eq. S1 (black), and the fitted-polynomial estimate of the quasi-static thermocline depth h'_{qs} (t) (red). (b) Temperature $T(h'_{qs}(t))$ at the depth $h'_{qs}(t)$ (blue) and its polynomial fit $T_{TC}(t)$ (red).*

In the second stage of determining $h(t)$, we first least-squares fit the undulating $h'(t)$ (black trace in Fig. S1a) with a third-order polynomial (red trace in Fig. S1a) to represent the quasi-static thermocline depth $h'_{qs}(t)$. Such a low-order polynomial fitted to $h'(t)$ over an entire season is relatively immune to the occasional inaccuracy in $h'(t)$. Then, examining each temperature profile at time t in the data set $T(z, t)$, we determine the temperature at depth $z=h_{qs}'(t)$ to construct the undulating temperature-time-series $T(h_{qs}'(t))$ at the quasi-static thermocline depth (Fig. S1b, blue trace). Fitting another polynomial to this undulating $T(h_{qs}'(t))$ gives the slowly varying temperature $T_{TC}(t)$ at the slowly evolving thermocline depth in the absence of internal waves (Fig. S1b, red trace). Finally, again time-stepping through the profiles in $T(z, t)$, the depth $\mathcal{Z}$ was determined for each t at which T_{TC} occurs to construct $\mathcal{Z}(T_{TC}(t)) \equiv h(t)$. Plots of $h(t)$ for both Owasco and Seneca Lakes appear in Fig. S2 as black traces, superposed on heat maps of the time-dependent temperature profiles $T(z,t)$. Note, because $h(t)$ corresponds to the instantaneous depth of the thermocline's quasi-static temperature $T_{TC}(t)$, it is analogous to an isotherm, but with the temperature of the "isotherm" allowed to vary to follow the seasonally changing temperature at the thermocline. The slowly varying thermocline depths $h_{1qs}(t)$, as fitted for both lakes with the damped-oscillator model, are also plotted in Fig. S2 (white traces).

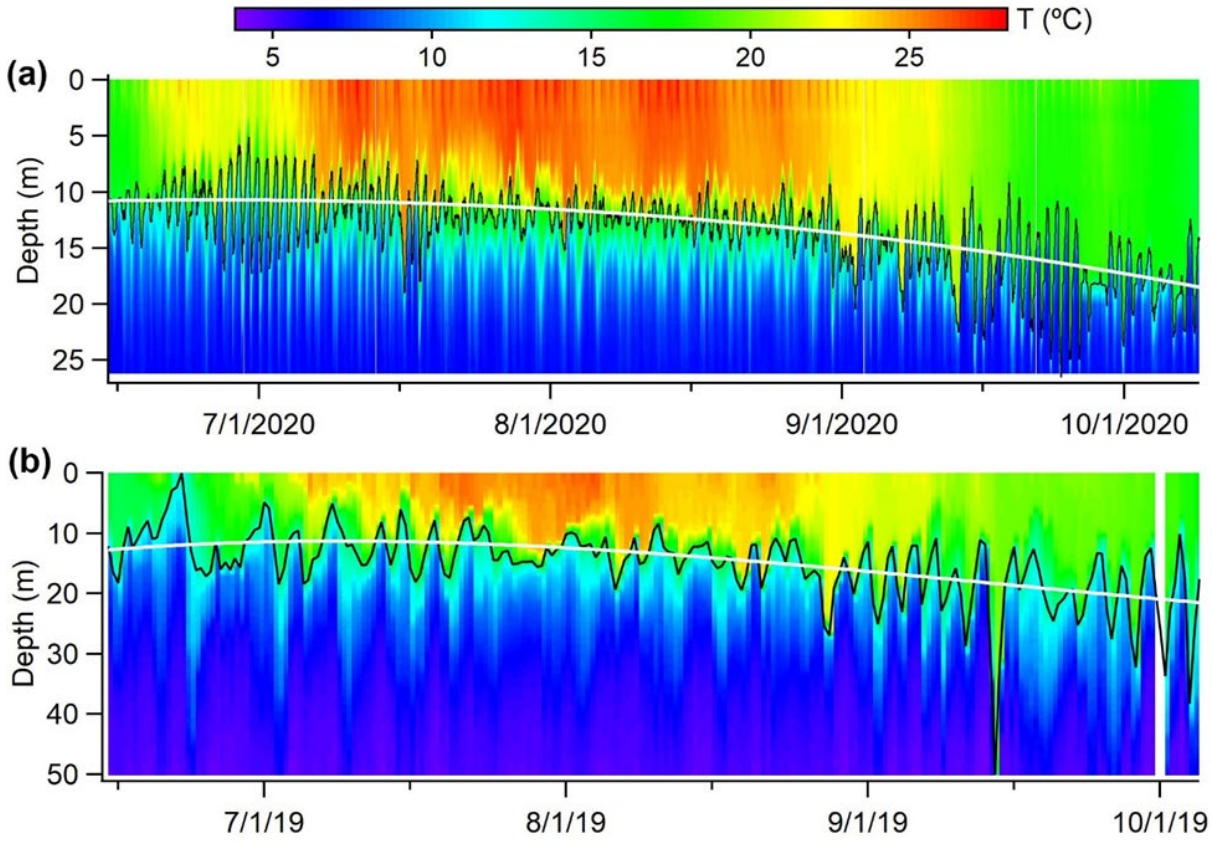

Fig. S2 *Heat maps of the temperature profiles T(z,t) for (a) Owasco Lake and (b) Seneca Lake (Finger Lakes Institute station). Also plotted are the instantaneous thermocline depths h(t) (black traces) and the quasistatic depths (white traces) represented by a polynomial during the fitting process.*

We found that $h'(t)$ gave results quantitatively similar to $h(t)$ in all further analysis except, as noted above, for the GLERL data. For consistency, all data were analyzed using the more elaborately obtained $h(t)$.

Equation of motion

Equation 1 of the main text gives the differential equation for the displacement ζ_n of a damped-harmonic-oscillator (Thornton and Marion 2008) that serves as an analog for the H*n* horizontal mode of the internal seiche. For completeness, the equation is reproduced here (but without offset t-t_0 on the right-hand side as used in the main text to treat field data):

$$\ddot{\zeta}_n(t) + 2\gamma\dot{\zeta}_n(t) + \omega_n^2\zeta_n(t) = \frac{4h_2}{\rho_2 LH}\rho_a C_D(t)U_{10}^2(t)\cos(\theta+\varphi), \qquad \text{(S2)}$$

Symbols in Eq. S2 are defined in the main text, and in Tables S1 and S2. Within reasonable approximations, Eq. S2 can be obtained from the hydrostatic treatment by Heaps and Ramsbottom (1966) of an ideal rectangular basin discontinuously stratified into two layers of constant thickness and weakly (i.e. linearly) driven by a uniform wind stress. In their theory of the coupled motions of the surface- and internal-seiche horizontal modes, these authors derive four coupled differential equations (their Eq. 76) in terms of the amplitudes of vertical motion of the surface and internal seiches, together with the amplitudes of the depth-averaged horizontal currents in the top and bottom layers. One can manipulate the four expressions constituting their Eq. 76 into exactly our Eq. S2 by (i) making the approximation that one can neglect the vertical acceleration of the lake's surface relative to the vertical acceleration of the thermocline; (ii) judiciously assuming $\rho_1 \approx \rho_2$; (iii) identifying their damping coefficient kh_1/H with our γ (here k is Heaps and Ramsbottom's phenomenological coefficient of friction between the current in the lower layer and the basin floor); and (iv) employing the coefficient for the H1-mode amplitude in their modal expansion for the thermocline displacement under a uniform wind-stress.

Computing the surficial wind stress $\rho_a C_D(t)U_{10}^2(t)$ that appears in Eq. S2 requires determining U_{10} and C_D, which is itself a function of U_{10}. The measured windspeed $U(t)$ was converted to $U_{10}(t)$ with a formula from Cole and Wells (2006) pertinent to a neutrally stable atmosphere: $U_{10}(t) = U(t)\ln(10/z_0)/\ln(z/z_0)$, with z=3.1 m, the height of the anemometers above the water in both FLI buoys, and the roughness z_0 set to 0.9 mm when the measured windspeed was below 2.235 m/s, and to 4.6 mm when above. The dimensionless drag coefficient C_D was computed following Wüest and Lorke (2003), who showed in their Fig. 3 that for $U_{10} \lesssim 5$ m/s, C_D follows a power law $C_D = 0.0044U_{10}^{-1.15}$, and for $U_{10} \gtrsim 5$ m/s, C_D increases following "Charnock's law," in which C_D is found from the implicit equation $C_D \approx [ln(10g/C_D U_{10}^2)/0.41 + 11.3]^{-2}$, where g is the acceleration of gravity and 10 has units of m. To aid computer calculations, we formed a composite curve for C_D comprising two curves, one being the power law when $U_{10} < 3.8$ m/s, and the other being Charnock's law when $U_{10} \geq 3.8$ m/s (the two curves cross at ~3.8 m/s), and then fitted the composite curve with a single formula (Yuan, 2009) to arrive at $C_D(U_{10}) = -0.00609 + 0.00577U_{10}^{-1.036} + 0.00462U_{10}^{0.171}$. For the atmospheric density, we used specifications for the U.S. Standard Atmosphere (NOAA 1976) to compute ρ_a=1.18 kg/m^3 at 21°C, the mean temperature measured by the FLI buoys over the stratified season (June 1 through October 1). This value is applicable to the elevations of both Seneca and Owasco Lakes (135 m and 217 m above sea level, respectively).

Variable-frequency Green's function

If one knows the Green's function $G_n(t,t')$ for the damped-oscillator differential equation, then the particular solution of Eq. S2 for a time-varying spatially uniform wind-stress is obtained via the convolution:

$$\zeta_n(t) = \frac{4h_2}{\rho_2 LH}\int_{-\infty}^{t} \rho_a C_D(t^{'}) U_{10}^2(t') G_n(t,t') dt'. \tag{S3}$$

In practice, the convolution's lower limit is set to t-T, where T=8 days for Owasco Lake, and 11 days for Seneca. The Green's function for a damped oscillator with *fixed* frequency is known (e.g., Hauser 1965), and was employed to analyze internal waves by Imam et. al. (2013), who call it the impulse function. The Green's function for a variable-frequency harmonic oscillator that is *undamped* is also known (Hiraiwa et al. 2020). Here we extend the derivation of Hiraiwa et al. to the case of a *damped* harmonic-oscillator with a slowly varying natural frequency $\omega_n(t)$. A prescription for the Green's function, obtainable via the variation of parameters, is given by (Hiraiwa et al. 2020):

$$G(t,t') = \frac{y_1(t')y_2(t) - y_1(t)y_2(t')}{y_1(t')\dot{y}_2(t') - \dot{y}_1(t')y_2(t')}, \tag{S4}$$

where $y_1(t)$ and $y_2(t)$ are independent solutions of the homogeneous damped-oscillator differential-equation (i.e., Eq. S2 with the right-hand side set to 0).

Following Hiraiwa et al. (2020), we seek approximations to $y_1(t)$ and $y_2(t)$ appearing in Eq. S4 by substituting the trial solution $y(t)=a(t)\exp(-\gamma t)\exp(i\phi(t))$ into the homogeneous form of Eq. S2, where we take γ, $\phi(t)$, and $a(t)$ to be real valued. After carrying out the differentiations of Eq. S2, and separating the real and imaginary parts of the resulting equation, one obtains two coupled equations in $a(t)$ and $\phi(t)$:

$$\ddot{a}(t) - a(t)\dot{\phi}^2(t) + a(t)(\omega_n^2(t) - \gamma^2) = 0 \tag{S5a}$$

$$2\dot{a}(t)\dot{\phi}(t) + a(t)\ddot{\phi}(t) = 0. \tag{S5b}$$

An approximate equation for $\dot{\phi}(t)$ can be found by dividing both sides of Eq. S5a by $a(t)$ and neglecting $\ddot{a}(t)/a(t)$ with respect to $\omega_n^2(t) - \gamma^2 \equiv \omega_{n\gamma}^2$, the frequency of the impulsively excited damped oscillator (Thornton and Marion 2008). This presumes that the envelope function $a(t)$ varies slowly relative to the oscillations of the oscillator (Sommerfeld 1964). Integrating the resulting first-order equation in $\dot{\phi}(t)$ then gives $\phi(t) = \phi_0 \pm \int_0^t \sqrt{\omega_n^2(t') - \gamma^2}\, dt'$. Using this solution for $\phi(t)$, Eq. S5b can be solved to give $a(t)=\kappa/(\omega_n^2(t)-\gamma)^{1/4}$, where κ is a constant. With this result for $a(t)$, the assumption above that $\ddot{a}(t)/a(t) \ll \omega_{n\gamma}^2$ is equivalent to assuming that the change in $\omega_{n\gamma}$ over a period is small compared to $\omega_{n\gamma}$. Substituting the formulas for $\phi(t)$ and $a(t)$ into the trial solution gives the two

independent solutions we seek:

$$y_n(t) = \frac{\kappa}{(\omega_n^2(t) - \gamma^2)^{\frac{1}{4}}} e^{i(\varphi_0 \pm \int_0^t \sqrt{\omega_n^2(t') - \gamma^2} dt')} e^{-\gamma t}, \tag{S6}$$

where the subscript n, either 1 or 2, corresponds respectively to the plus- or minus-signed phase in the exponent. Substituting $y_1(t)$ and $y_2(t)$ from Eq. S6 into Eq. S4 leads to:

$$G_n(t, t') = \frac{e^{-\gamma(t-t')}}{(\omega_n^2(t) - \gamma^2)^{1/4}(\omega_n^2(t') - \gamma^2)^{1/4}} sin \int_{t'}^{t} \sqrt{\omega_n^2(t'') - \gamma^2} dt''. \tag{S7}$$

We note that if there is no damping (γ=0), Eq. S7 reduces to the result given by Hiraiwa et al. (2020) for an undamped oscillator with variable frequency. Similarly, if ω_n is not a function of time, Eq. S7 reduces to the known Green's function for a damped oscillator with a constant natural frequency.

Initial values

To reliably converge, the algorithm to fit $h_{LP}(t)$ with the fitting function $\mathcal{F}(t)$ (Eq. 2) requires seeding with a set of initial fitting-parameters reasonably close to their final fitted values. The function $\mathcal{F}(t)$ contains two polynomials, $P_{qs}(t)$ representing the slowly deepening quasi-static thermocline, and $f_1(t)$ representing the seasonally varying natural frequency of the H1 internal seiche. For the initial values of the polynomial coefficients of $P_{qs}(t)$, we use the coefficients of a third-order polynomial fitted directly to the thermocline depth $h(t)$. For the initial values of the polynomial representing $f_1(t)$, we use the coefficients of a polynomial fitted to a time-series of frequency, $f_{M1}(t)$, computed over the season with the modified Merian equation (Heaps and Ramsbottom 1966; Mortimer 1974):

$$f_{Mn} = \frac{n}{2L} \sqrt{\frac{g' h_1 h_2}{H}}. \tag{S8}$$

Here, g'=$g(\rho_2$-$\rho_1)/\rho_2$, where g is the acceleration of gravity, 9.8 m/s^2, and ρ_1 and ρ_2 are the densities, respectively, of the upper and lower layers in the two-layer model. These densities are estimated by depth averaging the density profiles from the surface to $h(t)$ for ρ_1, and, for ρ_2, from $h(t)$ to the baroclinic depth H. The density ρ_2 below the deepest employed sensor is taken to be that at the sensor. To evaluate Eq. S8, h_1 is replaced by $h(t)$, and h_2 by H- $h(t)$. A representative result for $f_{M1}(t)$ is presented as a red trace in Fig. S3 for the Seneca Lake 2019 season; the blue trace shows a third-order polynomial fit, the coefficients of which, after multiplying by 2π, were used as the initial fitting coefficients for $\omega_1(t)$=$2\pi f_1(t)$ in the Green's function of Eq. S7.

Internal seiche degeneration

The formulas in the last column of Table S3 give decay times for the internal seiche caused by viscous damping (characterized by a time T_d), and by nonlinear degeneration into surges (T_s), Kelvin Helmholtz billows (T_{KH}), and bores (T_b). The formulas were obtained by combining a set of expressions compiled in a seminal paper by Horn et al. (2001) that are tabulated in columns three through five. The expressions pertain to the idealized two-layer model that is subjected to the sudden onset of a constant and uniform wind at t=0 lasting longer than P/4, where P is the period of the H1 internal seiche. In deriving the last column, we assumed the basin volume $V=A_bLH$; set $P=1/f_{M1}$, with f_{M1} given by Eq. S8, and used Eq. S8 to eliminate g'. For field evaluation of the formulas in the last column, we set $P=1/f_1$, where f_1 is the fitted H1 frequency.

The parameter η_0 in Table S3 is the amplitude at a basin endwall of the undulating internal seiche (comprising all excited Hn modes). To estimate field values for η_0, we first pick out the maxima and minima of the undulating time-series $\delta h_{LP}(t)$ (Fig. 2). To better conform to the definition of η_0 as requiring a wind duration of at least P/4, extrema in $\delta h_{LP}(t)$ are excluded that occur less than P/4 since $\delta h_{LP}(t)$ last crossed zero. The selected extrema serve as a measure of the H1 amplitude A at the field station, which was converted to η_0 through the relation $\eta_0=(\pi^2/8)[A/\cos(\pi d/L)]$, where the term in square brackets gives the H1 amplitude at the basin endwall nearest the station a distance d away, assuming an ideal cosine profile for the H1 mode. The factor $\pi^2/8$ converts the endwall H1-amplitude to the amplitude comprising all Hn modes excited by a uniform wind (Boegman et al. 2005). The basin endwalls were located at the endpoints of the baroclinic length, i.e., where the lake bottom intersects the seasonal-mean depth of the thermocline, giving d=0.8 km for the USGS station on Owasco Lake and d=4.0 km for the FLI buoy on Seneca Lake. Data from these two stations are used to estimate the times T_d and T_s plotted over a season in the main text (Fig. 5), and T_{KH}, and T_b plotted in Fig. S4.

The formula for T_d in terms of U_{max} and a bottom boundary-layer thickness δ_b was first proposed by Spigel and Imberger (1980), who also recommended an empirical formula for δ_b based on measurements by Kalkanis (1964). In Table S3, following Heaps and Ramsbottom (1966), U_{max} was set to the formula for the maximum value of U_2, the depth-averaged current in the lower layer, but note that others have set U_{max} to $|U_2\text{-}U_1|$, the maximum relative shear-velocity between depth-averaged upper and lower layers (Spigel and Imberger 1980; Dorostkar and Boegman 2013). The difference can be substantial for deep lakes since $|U_2|=(h_1/H)|U_2\text{-}U_1|$ (Horn et al. 2001).

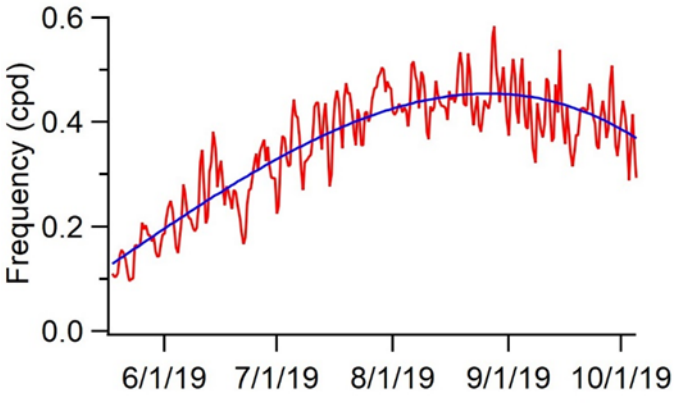

Fig. S3 *The internal-seiche frequency $f_{M1}(t)$ computed with Eq. S8 for Seneca Lake (red) trace, and the third-order polynomial fit used as an initial guess when fitting the damped-oscillator model (blue curve).*

The selection of one velocity or the other underscores that an analytical formula provides only a rough estimate of T_d, since the viscous loss-rate depends on the actual (not depth-averaged) current at the bottom boundary-layer (Gloor et al. 2000), and on the shape of the basin (Fricker and Nepf 2000).

A bore or billow is unable to form in the two-layer model if T_b or T_{KH} exceeds $P/4$, the time it takes the oscillating current of a seiche with period P to grow from zero to its maximum speed before receding again. Figure S4 compares the computed formation times T_b and T_{TK} to the $P/4$ threshold for Owasco and Seneca Lakes. It appears that these turbulent interfacial-modes rarely occur in Owasco Lake. However, for Seneca Lake, both T_b and T_{KH} occasionally fall on or below the threshold, indicating that these modes may occur briefly during the strongest thermocline displacements. Likewise, with the aid of three-dimensional modeling, Dorostkar and Boegman (2013) reported field evidence for the presence of bores in Cayuga Lake, which is located between Seneca and Owasco Lakes, and is of comparable size to Seneca Lake.

Table S3 Internal-seiche decay mechanisms, and time scales that determine which are relevant. All formulas excepting the final column are from Horn et al. (2001).

Loss mechanism; characteristic time	Relevant when:	Formula	Sub-expression	Sub-expression	Formula after eliminating g' via Eq. S8
Viscous loss at the bed boundary; T_d	$T_d < T_s$	$T_d = \frac{PV}{\delta_b A_b}$	$\delta_b = \frac{U_{max} e}{471}\sqrt{\frac{P}{\nu}}$	$U_{max} = g' \frac{h_1}{H}\frac{\eta_0}{L}\frac{P}{2}$	$T_d = \frac{236 h_2 H \sqrt{\nu P}}{eL}\frac{P}{\eta_0}$
Thermocline slope steepens into a surge front; T_s	$T_s < T_d$	$T_s = \frac{L}{\lvert\alpha\rvert\eta_0}$	$\alpha = \frac{3}{2} c_0 \frac{h_1 - h_2}{h_1 h_2}$	$c_0 = \sqrt{\frac{g' h_1 h_2}{H}}$	$T_s = \frac{h_1 h_2}{3\lvert(h_1 - h_2)\rvert}\frac{P}{\eta_0}$
Formation of Kelvin-Helmholtz billows at the thermocline; T_{KH}	$T_{KH} < \frac{P}{4}$	$T_{KH} = \frac{L}{\eta_0}\sqrt{\frac{\delta_\rho}{g'}}$			$T_{KH} = \frac{1}{2}\sqrt{\frac{\delta_\rho h_1 h_2}{H}}\frac{P}{\eta_0}$
Bore formation at the thermocline; T_b	$T_b < \frac{P}{4}$	$T_b = \frac{P}{4}\frac{h_1}{\eta_0}\sqrt{\frac{H h_2^2}{h_1^3 + h_2^3}}$			$T_b = \frac{h_1}{4}\sqrt{\frac{H h_2^2}{h_1^3 + h_2^3}}\frac{P}{\eta_0}$

P is the period of the H1 internal seiche, evaluated as explained in the text; δ_b is the thickness of the turbulent bottom boundary layer; A_b is the basin bed area; U_{max} is a maximum velocity in the two-layer model, taken in this report to be that of the lower layer; e is the bottom roughness, assumed to be 0.06 m; ν is the kinematic viscosity of the bottom layer, assumed to be the viscosity at 6°C, or 1.27×10^{-6} m^2/s; α is the nonlinear coefficient appearing in the Kortweg-deVries equation; c_0 is the phase velocity of the counterpropagating waves that form the internal-seiche standing wave; δ_ρ is the thickness of the metalimnion, set in both lakes to 5 m to match its average thickness estimated by eye from temperature profiles; h_1 and h_2 are, respectively, the thicknesses of the upper and lower layers; $g' = g(\rho_2 - \rho_1)/\rho_2$, where g is the acceleration of gravity, 9.8 m/s^2, and ρ_1 and ρ_2 are, respectively, the densities of the upper and lower layers; and η_0 is the internal seiche amplitude (sum of all Hn modes) at a basin endwall.

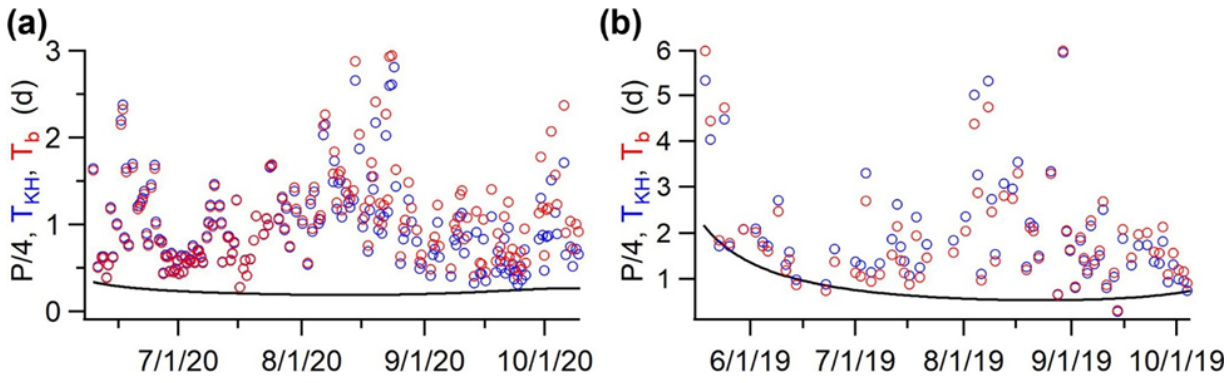

Fig. S4 *Computed formation times for Kelvin-Helmholtz billows (T_{KH}; blue) and bores (T_b; red) in (a) Owasco Lake and (b) Seneca Lake compared to a quarter of the fitted seiche period P/4 (black traces). These nonlinear modes are unable to birth if their formation times lie above the P/4 threshold.*

References

Boegman, L., G. N. Ivey, and J. Imberger. 2005. The energetics of large-scale internal wave degeneration in lakes. Journal of Fluid Mechanics **531**: 159–180. doi:10.1017/S0022112005003915

Cole, T. M., and S. A. Wells. 2006. CE-QUAL-W2: A Two-dimensional, Laterally Averaged, Hydrodynamic and Water Quality Model, Averaged, Hydrodynamic and Water Quality Model, Version 3.5 Version 3.5. Instruction report EL-06-1. EL-06-1 U.S. Army Corps of Engineers.

Cossu, R., and M. G. Wells. 2013. The Interaction of Large Amplitude Internal Seiches with a Shallow Sloping Lakebed: Observations of Benthic Turbulence in Lake Simcoe, Ontario, Canada. PLoS ONE **8**: e57444. doi:doi.org/10.1371/journal.pone.0057444

Dorostkar, A., and L. Boegman. 2013. Internal hydraulic jumps in a long narrow lake. Limnol. Oceanogr. **58**: 153–172. doi:10.4319/lo.2013.58.1.0153

Fricker, P. D., and H. M. Nepf. 2000. Bathymetry, stratification, and internal seiche structure. Journal of Geophysical Research: Oceans **105**: 14237–14251. doi:https://doi.org/10.1029/2000JC900060

Gloor, M., A. Wüest, and D. M. Imboden. 2000. Dynamics of mixed bottom boundary layers and its implications for diapycnal transport in a stratified, natural water basin. Journal of Geophysical Research: Oceans **105**: 8629–8646. doi:10.1029/1999JC900303

Hauser, W. 1965. Introduction to the Principles of Mechanics, Addison-Wesley.

Heaps, N. S., and A. E. Ramsbottom. 1966. Wind effects on the water in a narrow two-layered lake. Philosophical Transactions of the Royal Society of London. Series A, Mathematical and Physical Sciences. Philosophical Transactions of the Royal Society of London **259**: 391–430. doi:10.1098/rsta.1966.0021

Hiraiwa, T., K. Soutome, and H. Tanaka. 2020. Forced harmonic oscillator interpreted as diffraction of light. Phys. Rev. E **102**: 032211. doi:https://doi.org/10.1103/PhysRevE.102.032211

Horn, D. A., J. Imberger, and G. N. Ivey. 2001. The degeneration of large-scale interfacial gravity waves in lakes. Journal of Fluid Mechanics **434**: 181–207. doi:10.1017/S0022112001003536

Imam, Y. E., B. Laval, R. Pieters, and G. Lawrence. 2013. The strongly damped baroclinic response to wind in a multibasin reservoir. Limnology and Oceanography **58**: 1243–1258. doi:10.4319/lo.2013.58.4.1243

Jones, F. E., and G. L. Harris. 1992. TS-90 density of water formulation for volumetric standards calibration. J. Res. Natl. Inst. Stand. Technol. **97**: 335.

Kalkanis, G. 1964. Transportation of bed material due to wave action. Technical Memorandum No. 2. Technical Memorandum No. 2 U.S. Army Corps of Engineers.

Mortimer, C. H. 1974. Lake hydrodynamics. Internationale Vereinigung für Theoretische und Angewandte Limnologie: Mitteilungen **20**: 124–197. doi:10.1080/05384680.1974.11923886

NOAA. 1976. U.S. Standard Atmosphere, 1976. NOAA-S/T-76-1562. NOAA-S/T-76-1562 National Oceanic and Atmospheric Administration.

Patterson, J. C., P. F. Hamblin, and J. Imberger. 1984. Classification and dynamic simulation of the vertical density structure of lakes. Limnol. Oceanogr. **29**: 845–861. doi:https://doi.org/10.4319/lo.1984.29.4.0845

Sommerfeld, A. 1964. Lectures on Theoretical Physics Volume IV: Optics, Academic Press.

Spigel, R. H., and J. Imberger. 1980. The classification of Mixed-Layer Dynamics of Lakes of Small to Medium Size. Journal of Physical Oceanography **10**: 1104–1121. doi:10.1175/1520-0485(1980)010<1104:TCOMLD>2.0.CO;2

Stevens, C., G. Lawrence, P. Hamblin, and E. Carmack. 1996. Wind forcing of internal waves in a long narrow stratified lake. Dyn. Atmos. Oceans **24**: 41–50. doi:10.1016/0377-0265(95)00409-2

Thornton, S. T., and J. B. Marion. 2008. Classical Dynamics of Particles and Systems, 5th ed. Centage Learning.

Wüest, A., and A. Lorke. 2003. Small-scale hydrodynamics in lakes. Annu. Rev. Fluid Mech. **35**: 373–412. doi:10.1146/annurev.fluid.35.101101.161220

Yuan, S. 2009. Comparison of Wind Stress Algorithms, Datasets and Oceanic Power Input. M.Sc. thesis. Mass. Inst. Technol.